Synthesis and Characterization of nanostructured α-MnO$_2$ electrodes for Supercapacitors Applications

By

Sello Simon Mothoa

A thesis submitted in fulfilment of the requirements for the degree of MSc in Chemistry in the Department of Chemistry, University of the Western Cape

Supervisor: Dr. S. Ji

Co-Supervisor: Prof. D. Key and Dr. R. Mohamed

November 2010

Declaration

I declare that "*Synthesis and characterizations of nanostructured α-MnO$_2$ electrodes for supercapacitors application*" is my own work and that it has not been submitted for any degree or examination in any other university, and that all the sources that I have used or quoted have been indicated and acknowledged by complete references
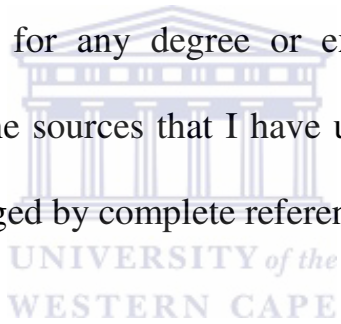
Sello Simon Mothoa   November, 2010

Signed………………………………

Acknowledgements

My first gratitude goes to the Almighty God, without Him I wouldn't be where I am today in my life. May His Grace and light continue to shine upon us.

Greatest appreciation goes to my parents Mr and Mrs Mothoa for their unconditional love and their support throughout my life. Not forgetting my two lovely sisters and all members of my extended family.

Special Thanks to my supervisor Dr. S. Ji for your guidance and support throughout the duration of this research, and not forgetting the co-supervisor Dr. Rushanah Mohamed.

Deepest gratitude to Prof. Key and Prof. V. Linkov for giving me a chance to conduct my research under South African Institute for Material Science (SAIAMC) and not forgetting all the staff members of the institute.

Thank you to Adrian Joseph (Department of Physics, UWC) for TEM analysis, to Dr. Remy Butcher (Material research group, iThemba Labs) for XRD analysis and Miranda Waldron (Electron unit microscope, UCT) for SEM and EDS analysis.

Last but not least, a warm thanks to my colleagues; thank you for your guidance, friendliness and encouragement guys, I will never forget you.

Abstract

The objective of this research was to develop highly efficient and yet effective MnO_2 electrode materials for supercapacitors applications. Most attention had focussed on MnO_2 as a candidate for pseudo-capacitor, due to the low cost of the raw material and the fact that manganese is more environmental friendly than any other transition metal oxide system. The surface area and pore distribution of MnO_2 can be controlled by adjusting the reaction time. The MnO_2 synthesised under optimum conditions display high capacitance, and exhibit good cycle profile.

This work investigates the ways in which different morphological structures and pore sizes can affect the effective capacitance. Various α-MnO_2 were successfully synthesised under low temperature conditions of 70 ^{o}C and hydrothermal conditions at 120 ^{o}C. The reaction time was varied from 1 to 6 hours to optimise the conditions. $KMnO_4$ was reduced by $MnCl.H_2O$ under low temperature, whereas $MnSO_4.4H_2O$, $(NH_4)_2S_2O_8$ and $(NH_4)_2SO_4$ were co-precipitated under hydrothermal conditions in a taflon autoclave to synthesise various α-MnO_2 nano-structures.

The effect of varying reaction time of MnO_2 synthesis and the formation mechanisms of the nanorods were investigated by using XRD, SEM and TEM. The results revealed the evolvements of morphologies ranging from brushy spherical morphologies to nanorods depending upon the reaction time. The surface area of the synthesised MnO_2 under low temperature conditions after 1, 3 and 6 hrs was 130.38, 129.2 and 127.08 m^2/g respectively; and was higher than for the samples synthesised under hydrothermal conditions, which could only reach 54.97, 33.45 and 60.17 m^2/g respectively. This was due to the indifference in morphological structures of various products under different synthesis conditions.

The electrochemical properties of the products were evaluated using cyclic voltammetry and galvanostatic charge-discharge testing. The MnO_2 synthesised under low temperature conditions showed higher capacitance values, with the sample obtained at low temperature reaction for 6 hour showing the maximum capacitance. In addition long life cycles and excellent stability were also demonstrated. The samples that were synthesised under hydrothermal conditions showed excellent long-term stability as compared to those synthesised under low temperature conditions, with the 1 hour sample achieving 70% efficiency of the first cycle and the 6 hour sample 63%.

In order to study more characteristic features of MnO_2 and for comparisons, the commercially purchased MnO_2 was also studied by using the above mentioned techniques as the baseline. The XRD analyses showed the nano-structured electrode material to have peaks with pattern that match the γ-MnO_2 polymorph. The peaks of the material were clear and very intense, showing the good purity of the electrode material. The agglomeration of the material showed spherical aggregates in the SEM analysis, the elemental composition of the material showed it contains only the Mn and O atoms in the ratio of 1:2. The pseudo-capacitance was determined via the cyclic voltammetry under different scan rates, to establish the influence of the scan rate on the specific capacitance of the material. The 5 mV/s scan rate exhibited the ideal specific capacitance of 88.1 F/g, the 50 mV/s scan rate exhibited 53.48 F/g, which agreed to the theory that at slower scan rates the electrolytic ions are inserted at all available pores and the electrode surface, resulting in an ideal capacitance. The charge-discharge tests of the electrode materials showed that they exhibit life cycles but poor stability. With the first cycle yielding the specific capacitance of 78.4F/g and the 100th cycle yielding just 13.6F/g, meant it gave only 17% of the first cycle. This showed that the γ-MnO_2 form is the least stable polymorphs of the manganese oxides.

List of Figures

List of Tables

List of Abbreviations

SC   Supercapacitors

EV   Electric Vehicles

HEV   Hybrid electric Vehicles

FCV   Fuel cell vehicles

ICV   Internal combustion vehicle

DLC   Double layer capacitor

EDL   Electron double layer

OHP   Outer Helmholtz plane

IHP   Inner Helmholtz plane

SEM   Scanning Electron Microscopy

TEM   Transmission Electron Microscopy

EDS   Electron Dispersive Spectroscopy

XRD   X-ray Diffraction

LT   Low Temperature Conditions

HT   Hydrothermal Conditions

CV   Cyclic Voltammetry
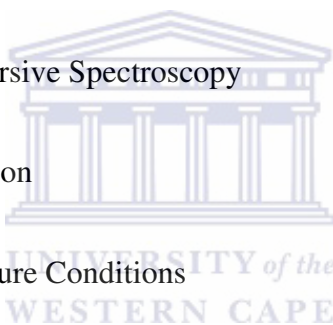
Table of Contents

Chapter 1: Introduction

1.1 Problem Identification

In recent years, as the movement for environmental protection is increasingly dominant and the rapidly increasing price of oil is an undeniable reality, the automobile industry has been looking to introduce electric vehicles (EV), hybrid electric vehicles (HEV) and fuel cell vehicles (FCV), in place of conventional internal combustion vehicles (ICV) as early as possible. In this regard, development of advanced energy storage technologies for application in transportation has become one of the top priorities due to its role as a critical technology for practical use of EV, HEV and FCV.

Figure 1.1: *Images of HEV which consists of IC engine and SC [1].*

EV, HEV and FCV are regarded as promising candidate to replace the ICV and would revolutionize the future transportation sector. EV, HEV and FCV have several advantages, such as low emissions, high fuel efficiency, good vehicle performance and low maintenance, over ICV. In the past decade, intensive effort has been put into

the R&D of EV, HEV and FCV technologies and significant progress in technologies has increased the prospects for EV, HEV and FCV application in transportation. The one of main barriers for EV, HEV and FCV commercialization in automobile industry is the high cost of energy storage unit used in these vehicles [1]. In the case of hybrid vehicle system, the high cost can be reduced by integrating new energy storage system into these vehicles. In this system, the power peak for acceleration and hill-climbing of the vehicle is provided by an energy storage system [1-8]. The super capacitor is a critical component for energy storage systems.

Super capacitors are electricity storage devices that have better reversibility and longer life cycles than batteries, and possess higher energy density as compared with conventional capacitors [8]. They have attracted much attention in many fields, e.g. hybrid power sources for EV, HEV and FCV, peak-power sources, backup-power systems, and supplementary power of fuel cells. The main application for super capacitors (SCs) is to use them as energy buffers to limit the power constraints on energy sources such as batteries and fuel cells [8-11].

Current research in supercapacitors has been mainly concentrated on the development of new electrode materials. High performance of supercapacitors lies in the nature and surface area of their electrodes. The nanomaterials with high surface and porosity are considered as the most promising electrode materials for supercapacitors. Consequently, the preparation and characterization of the high-surface-area nanomaterials such as nanowires and nanotubes have been being carried out extensively in the past few years. Among these nanostructures, α-MnO$_2$ nanomaterials

have attracted much attention because of their low cost, ease of synthesis, relatively high conductivities and nano-scale dimensions.

In this proposed project, nano-scale α-MnO$_2$ will be prepared electrochemically by a fast and environmentally friendly biomolecules-assisted method for supercapacitor application.

1.2 Research Background

Supercapacitors (SCs) are charge-storage devices. Compared to batteries they have high power density, more excellent reversibility and longer cycle life. Therefore SCs have played an increasingly important role in the fields of power source especially in automotive applications, such as electric and hybrid electric vehicles. The higher power density of SCs offers improved vehicle acceleration and the ability to recover more energy from regenerative braking, since they can be charged or discharged at higher current. Generally, the key for SCs is to achieve high specific power depends on the inheritance properties and the surface area of their electrode materials. Therefore, current researches in the field of supercapacitors have been carried out with increased emphasis on the development of new electrode materials.

The growing interest in supercapacitors has been stimulated by their potential application as electrical devices operating in parallel with the battery in electric vehicle to provide high power [12] [13]. The operational voltage per cell, limited only by the breakdown potential of the electrolyte is usually less than 1 or less than 3 volts per cell for aqueous or organic electrolytes respectively [14].

The concept of storing electrical energy in the electrical double layer that is formed at the interface between an electrolyte and a solid has been known since 1800 [14]. The

first electrical device using double layer charge storage was reported in 1957 by H.I Becker of General Electric (U.S Patent 2, 800, 616) [14]. Unfortunately, Becker's device was impractical in that, similarly to a flooded battery, both electrodes needed to be immersed in a container of electrolyte, and the material was never commercialised. Becker did, however, appreciate the large capacitance value subsequently achieved by Robert A. Rightmare, a chemist at the standard oil company of Ohio (SOHIO), to who can be attributed the invention of the device in the format now commonly used [14].

Whereas a regular capacitor consists of conductive foils and a dry separator, the supercapacitor crosses into battery technology by using special electrodes and some electrolyte. There are three types of electrode materials suitable for the supercapacitor. They are: high surface area activated carbons, metal oxide and conducting polymers. The high surface electrode material, also called Double Layer Capacitor (DLC), is least costly to manufacture and is the most common. It stores the energy in the double layer formed near the electrode surface.

Rather than operate as a main battery, supercapacitors are more commonly used as memory backup to bridge short power interruptions. Another application is improving the current handling of a battery. The supercapacitor is placed in parallel to the battery terminal and provides current boost on high load demands. The supercapacitor will also find a ready market for portable fuel cells to enhance peak-load performance. Because of its ability to rapidly charge, large supercapacitors are used for regenerative braking on vehicles. Up to 400 supercapacitors are connected in series to obtain the required storage energy

1.2.1 The concept of double layer

When an electrode, that is an electronic conductor is immersed into an electrolyte solution, that is an, ionic conductor, there is a spontaneous organization of charges at the surface of the electrode and in the electrolyte facing the electrode. The electron double layer (EDL) forms at the electrode-electrolyte interface with one layer at the surface inside the conductor and the other layer in the electrolyte as shown in figure 1.2 [15]. The two charged layers are considered to behave as a physical capacitor, with the charges in the solution and in the conductor separated by a distance of the order of molecular dimension. The characteristics of the EDL depend on the electrode surface structure, the composition of the electrolyte, and the potential field between the charges of the interface [15].
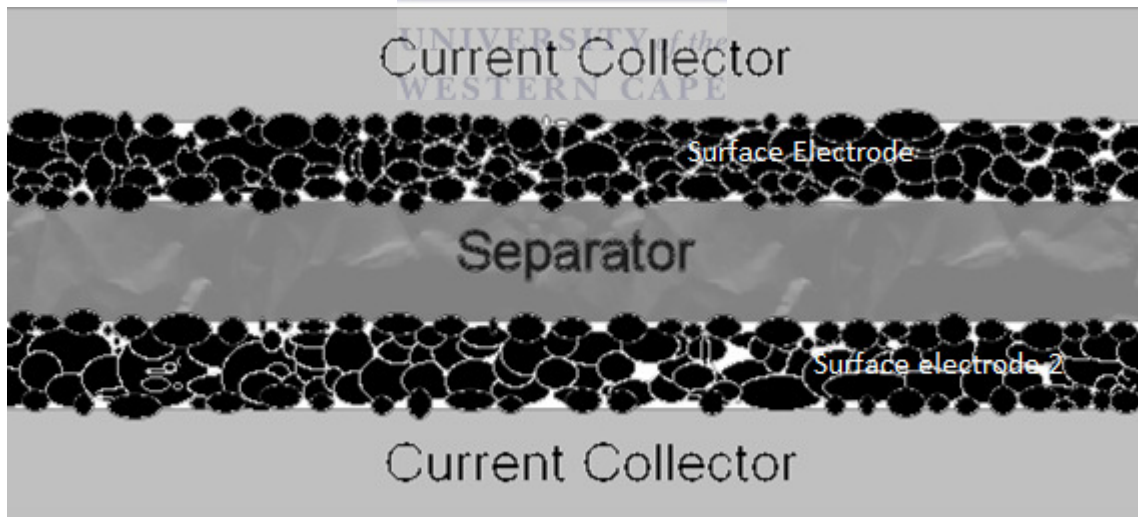
Figure 1.2: Schematic representation of the core elements of a typical supercapacitor [16].

Depending on the surface charge of the of the electrode materials, positive or negative ions from the electrolyte form the solution part of the EDL at the interface between the electrode and the electrolyte. A simplified structure is shown in figure 1.3

for the case of the negatively charged electrode surface. According to this simple Helmholtz model, the charges are concentrated on each side of the electrode surface. A more complex model of the EDL structure in figure 1.3 takes into account the different sizes of the ions and their reactivity with the surface. The outer Helmholtz plane (OHP) refers to the distance of closest approach of non-specifically adsorbed ions (generally cations) in solution. Cations that populate the OHP are usually solvated anions. The intercalations of the ions of the OHP with the surface charge have the character of coulombic interactions. The inner Helmholtz plane (IHP) refers to the distance of closest approach of specifically adsorbed ions (generally anions) and/or adsorbed solvent molecules to the electrode surface. These adsorption processes are determined by chemical affinities of the ions to the electrode surface and the field strength in the EDL. In practice, the structure of the EDL is much more complex than the models discussed above.
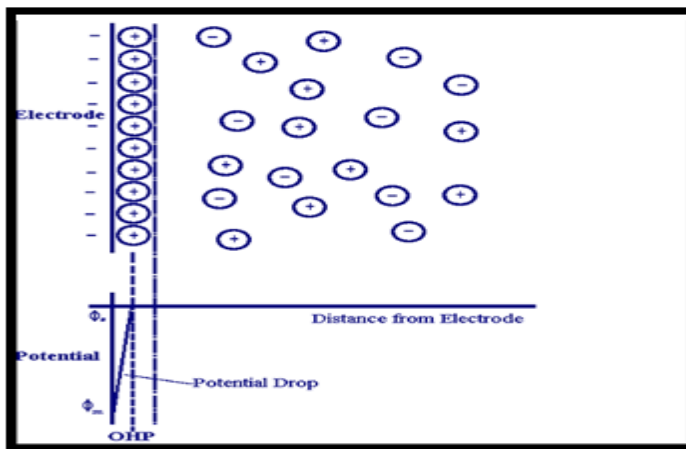
Figure 1.3: *Schematic diagram of electric double layer. The line marked OHP represents the outer helmotz plane, which is in line with the first row of ions with an opposite charge of the electrode [15].*

1.3 Research Aim

The foremost aim of this research is to prepare some highly efficient and cost effective electrode materials based on α-MnO_2 to improve electrochemical performance of electrochemical capacitors.

For the supercapacitors application, cost effectiveness, ease of synthesis, high surface area and environmental friendliness are the important requirements of nanostructured electrode materials. MnO_2 also shows a huge structural flexibility and appears in a number of crystallographic polymorphs such as α-, β-, γ-, δ-, and ε-MnO_2 [17]. Consequently, rational synthesis of MnO_2 materials with controllable crystal structures, morphologies and sizes is very important [17, 18]. The synthesis of nanostructured α-MnO_2 has reportedly been accomplished by various methods such as reduction, co-precipitation, sol-gel route, chemical decomposition and many more. The α-MnO_2 can be fabricated under many variable conditions including hydrothermal and low temperature, and the layered structure is suitable for use as a cathode material in supercapacitor cells since it does not transform into a spinel phase during a charge and discharge cycling, thus have a very good reversibility [18]. The α-MnO_2 product fabricated under these conditions contains water with a large channel of the structure; the water can be removed from the MnO_2 framework without degradation of the structure [18].

Materials will be analysed in terms of their structural and electrochemical properties in order to obtain a better understanding of the factors that control and affect capacitance and cyclability of MnO_2 insertion electrodes in SCs. The main focus of the study includes:

➢ Identification of cheap methods and materials which can be used for the synthesis of nanostructured MnO_2 electrode.

➢ The synthesis of nanostructured MnO_2 electrodes for applications in SCs which are;

- Highly conductive

- Highly stable

- Long life cycles and good reversibility

➢ Optimisation of the electrodes preparation methods;

➢ Characterisation of the synthesised electrodes by using various characterization techniques;

➢ Evaluation of which method produced MnO_2 electrodes with properties listed above;

➢ Assemble and optimise a small super capacitor with synthesised nanostructured α-MnO_2 as electrode.

1.4 Research Framework

- The first task was to identify the best method and conditions to prepare the nanostructured 1D MnO_2, which is foundation of the project. Two kinds of nanostructured 1D MnO_2 will be synthesized under various conditions to identify the best preparation method and followed by optimizing the conditions to obtain highly capacitance material. Electrode preparation and screening of their capacitance using electrochemical techniques will be carried out.

- The second task will be characterization of physical properties of electrodes like size and morphologies of the nanosized electrode materials using analytical methods. This will give an insight to the electrochemical behaviour of the nanostructure and will help to optimise the preparation conditions. Initially lot of characterization should be made to identify the best preparation method and during the project this will be used to characterise the best electrode obtained.

- The electrochemical capacitance of composite electrodes will be examined by cyclic voltammetry and charge discharge test. The specific capacitance value will be evaluated by these measurements.

- The super capacitor will be assembled and optimised using synthesised nanostructured MnO_2 as electrode to study and improve the electrochemical performance of the electrodes in the super capacitor cell.

1.5 Investigation Outline

Chapter 2: Literature Review: Synthesis of composites of MnO_2 materials.

- The literature review focuses on the discussion of MnO_2, their structure, synthesis and applications. Different approaches to synthesise and electrochemical behaviours of various forms are discussed. Important parameters that can influence the electrochemical behaviour of MnO_2 based materials are also summarised.

Chapter 3: Materials and Methods

- This chapter fundamentally serves as continuation of literature review, but with more emphasis given on the characterization techniques employed in the study. It also outlines the type of materials that are used.

Chapter 4: Results and Discussions

- Chapter 4 gives insight about synthesis of composite nanostructured MnO_2 materials. It starts with the discussions of synthesis of materials under various conditions namely; hydrothermal and low temperature conditions. This is then followed by discussing the morphological studies of the nanostructures using the SEM, TEM, EDS and XRD. Electrochemical characterization of the consolidated composite materials was studied by CV and charge-discharge test.
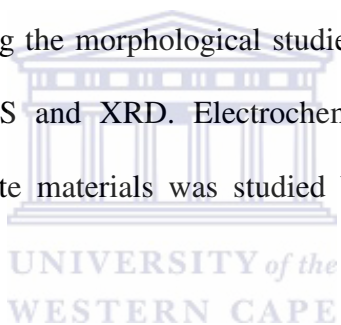
Chapter 5: Conclusions and Recommendations

- The study is concluded with a concise discussion of the objectives achieved in relation with the study of the novel nanostructured MnO_2 materials. Recommendations and possible future works are also discussed.

Chapter 2: Literature Review

2.1 Introduction

In the context of fossil fuel shortage and climate change, the production, conversion, storage and distribution of energy have become the focus of today's world. Owing to its unique power density and energy density range which fills the gap between batteries and traditional capacitor, supercapacitors (also known as electrochemical capacitors or ultracapacitors) play important roles in energy storage and efficiency [19, 20]. Typical electrode materials for supercapacitors include carbon, conducting polymers and transition metal oxides [20].

Metal oxides represent a type of attractive material with high specific capacitance, wide operational potential window and stability through charge-discharge cycling. Ruthenium oxide as an example can deliver relatively constant and appreciable capacitance of 600-1000 F g^{-1} with a potential window of 1.4V. However, the rarity of ruthenium in the earth's crust and hence the high market price of RuO_2 limits applications mostly in military and aerospace [19]. On the other hand, as the twelfth most abundant element on the earth [22], manganese is an inexpensive material with various oxidation states.

Manganese oxides (MnO_2) are a class of environmentally friendly material compared with other metal oxides, only harmful by excessive inhalation or imbibing [19, 22]. Throughout the years, MnO_2 in various forms has been widely studied as the electrode materials in various energy storage systems, such as alkaline batteries, lithium ion batteries and supercapacitors. In all these cases, MnO_2 has been proven to be a reliable electrode material with high performance [19].

MnO_2, as an environmentally friendly material with various oxidation states, have a long history as an electrode material for batteries. Recently, a new energy storage system, supercapacitor with its unique power density and energy density range, has been put in the focus [19]. With a vast number of ongoing researches in exploring MnO_2 as the electrode material for supercapacitor, this article provides a comprehensive review on the recent findings in this area. Different approaches to synthesise and the electrochemical behaviours of various forms of pure and composite MnO_2 were presented.

Important parameters that can influence the electrochemical behaviour of MnO_2 based materials are summarised. The state of the art of the engineering of MnO_2 into composite or specific nanostructure with improved electrochemical performance is reviewed. A brief summary on the performance of symmetric and hybrid supercapacitors with MnO_2 as electrode material is given. Appropriate cell configuration has been proven to be necessary for the optimisation of the capacitive performance. Moreover, the essential difference of charge storage mechanism between battery and supercapacitor for MnO_2 electrode is stated. Based on these literature findings, MnO_2 is believed to be a type of promising and competitive electrode material for applications in supercapacitors [19].

2.2 Energy storage in electrochemical double-layer capacitors (History)

The concept of the double layer was first studied by chemists since 19th century by von Helmotz when he developed the model of the double layer concept in

investigation of colloidal suspension [14]. This work was subsequently extended to the surface of metal electrodes in the late 19th and early-mid-20th centuries [14]. In 1957, the practical use of a double-layer capacitor, for the storage of electrical charge, was demonstrated and patented by General Electric [14]. This early patent utilised crude porous carbon electrodes in an aqueous electrolyte.

Not until the granting of a patent to SOHIO in 1966 was it acknowledged that these devices actually store energy in the electrical double-layer, at the interphase between electrode and solution [14]. The first commercial double-layer supercapacitors originated from SOHIO who went on to patent a disc-shaped device that consisted of carbon paste electrodes, formed by soaking porous carbon in an electrolyte separated by an ion-permeable separator [14]. SOHIO also utilized non-aqueous electrolytes in their early devices, but, a lack of sales saw them license their technology to NEC in 1971; who further developed and successfully marketed double-layer supercapacitors, primarily for memory backup applications [14]. These early devices typically had a low voltage and a high internal resistance.

By the 1980s a number of companies were producing double-layer capacitors, e.g., Matsushita (Gold capacitor), Elna (Dynacap) and PRI (PRI ultracapacitor), although the last-mentioned incorporated relatively expensive metal oxide electrodes, primarily targeted for military applications [14]. Today, a number of high-performance EDLC devices, based on porous carbons, are commercially available from a range of manufacturers and distributors around the world.

The earliest electrochemical capacitors introduced 30 years ago were symmetric designs (two identical electrodes) in aqueous electrolyte, H_2SO_4 or KOH, which

limited operating cell voltage to 1.2 V/cell and nominal cell rating to 0.9 V. In the second generation of electrochemical capacitors, the use of organic electrolyte-typically an ammonium salt dissolved in an organic solvent, such as propylene carbonate or acetonitrile-led to an increase of the rated cell voltage from about 0.9 V/cell to 2.3-2.7 V/cell. Spiral-wound or prismatic plate construction electrochemical capacitors using an organic electrolyte are the most popular type today [21].

2.3 Mechanism of Charge Storage

It was tested that within a certain potential range, MnO_2 can exhibit in good approximation rectangular cyclic voltammograms (CVs). Such behaviour differs from many usual charge transfer reaction on electrode, but it is in fact Faradaic in nature, i.e. the electrode processes involve electron transfer across the electrode/electrolyte interface [19]. However, the CVs also resemble in shape what is usually observed during the so called electrode double layer charging-discharging process in which electrons and ions are only accumulated on each side of the electrode/electrolyte interface; and such charge transfer related capacitor like behaviour has been generally described as pseudocapacitance. The associated capacitance value, i.e. the pseudo-capacitance can be derived from the CV data using the equation (2.1) below [19].

$$C = \frac{\Delta q}{\Delta E} = \frac{I}{v} \tag{2.1}$$

Where I is the current and v is the potential scan rate.

The two accepted hypotheses for charge storage mechanisms of MnO_2 in supercapacitors were proposed to be surface adsorption of electrolyte cations (M^+) on MnO_2 [23] and proton intercalation [24]. It was further suggested that both protons and alkali cations are involved in the redox process [25, 26], if the structure of the MnO_2 is not too dense for the diffusion of alkali cations [27]. A more specific statement was made that H_3O^+ plays the predominant role in all cases, while the extent of participation of alkali cations first decrease and then increases with ionic size [15], based on the research on finely grained $MnO_2.nH_2O$ thin film with ζ-MnO_2 type crystal structure in several aqueous alkali and alkaline salt solutions.

$$MnO_2 + M^+ + e^- \leftrightarrow MnO_2^- M^+ \qquad (2.2a)$$

Positive electrode

$$MnOOH \leftrightarrow HMnO_2 + H$$

Negative electrode

$$MnO_2 + \delta H^+ + \delta e \leftrightarrow H_\delta MnO_2 \qquad (2.2b)$$
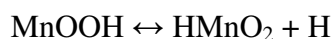
It is to be noted that MnO_2 has been widely used as an electrode material in both batteries material in both batteries and supercapacitors. The electrode reaction remain the same or similar in both devices, as described by equations (2.2 a) and (2.2b). However, in supercapacitors, the loading of MnO_2 on each electrode is usually less than a few tens of mg per cm^2 in mass or a few tens of µm in thickness. The consequences is that, in comparison with batteries supercapacitors have a smaller charge storage capacity, but a greater overall change transfer rate to enable high power performance [19].

Another important electrochemical feature of MnO_2 is its capacitor like charge-dischsrge characteristics, i.e. the extent of charge acceptance Δq changes linearly, or

almost linearly, with the change of potential ∆E [20]. This behaviour is described by equation (1)

The electron transfer processes in the classic chemically modified electrodes take place in very well separated redoxes active which are non-interactive with each other [19]. In other words, these localised redox active sites are equal or fairly close to each other in energy state, and hence accept or donate electrons at potentials very close to each other, leading to the peak shaped CV in a narrow potential range [19]. However, if these redox active sites are closely located in the surface layer of the electrode and hence interactive with each other, a broad range or band of energy states can form with negligibly small differences between the neighbouring states. Such a situation corresponds that in semiconductors, including most transition metal oxides, and is also comparable with electron delocalisation in conjugated chemical bonds, as in conducting polymers, resulting from overlapping electron orbits between neighbouring atoms. Consequently, electron transfer into each energy state in the broad band becomes continuous over a wide range of potentials, which is responsible for the constant current flow and hence the rectangular CV
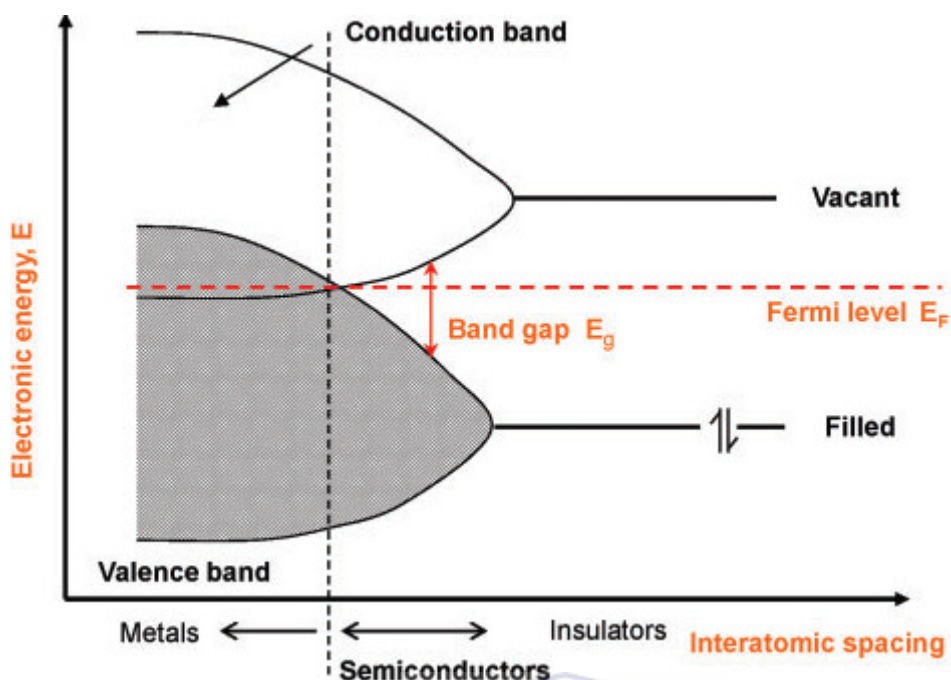
Figure 2.1 Schematic illustration of band theory [28].

The above analysis is derived from the semiconductor or band theory [28] which is quantitatively illustrated in figure 2.1. The right hand side of figure 2.1 represents the electron transfer energy states in isolated molecules and insulators, and can be compared with the classic chemically modified electrodes in which the redox active sites are well separated and only support localised electron transfer from the electrode substrate to each of the redox active sites and vice versa, but no electron conduction between any neighbouring sites.

The energy levels of the filled and vacant states are singular, corresponding to a fixed potential for electron transfer. The far left of Fig. 2.1 shows the continuous electron energy states from the fill valence band and vacant conduction band, enabling free electron mobility in response to an electrical field. In Fig. 2.1, semiconductors are featured by the separated filled valence band and the vacant conduction band. The energy gap between the lowest vacant and highest valence levels E_g is characteristic to each semiconductor. In a sufficiently high and increasing electrical field, continuous excitation of electrons from the valence band

to the conduction band occurs. This process produce free moving or delocalised electrons in the conduction band as well as mobile 'holes' in the valence band [28], leading to the continuous charge accumulation upon the application of the increasing potential, and hence the capacitive current.

Advanced technologies, including x-ray photoelectron spectroscopy (XPS), X-ray absorption near edge structure (XANES) technology and K edge X-ray absorption spectroscopy, have made it possible to identify the exact oxidation status and study the pseudocapacitive nature of charge storage in MnO_2. A progressive change of the Mn valence was observed when the potential decreased from 1.0 to 0 V [29] and the hysteresis of Mn oxidation state adjustment with respect to the applied potential was also revealed [30]. Manganese oxidation states for the reduced and oxidised forms during the charge-discharge process have been identified [27, 26] and more explicit observations of a continuous and reversible change in Mn oxidation state, from + 3.23 to 3.95 and then back to + 3.27 with potential cycling, were reported [30].

It is worth pointing out that deviation from the band theory can occur if the electrode process involves kinetic complications, for example, the influence of counter ion diffusion and ohmic polarisation. Thus, MnO_2 in the form of a thin coating, particularly porous, can behave like a capacitor. However, when it is used in a bulk quantity in batteries, the performance is largely controlled by the diffusion of the counter ions, and hence deviates from that of a capacitor [19].

2.4 Synthesis of Manganese dioxide

2.4.1 Chemical synthesis

Common chemical approaches to MnO_2 include reducing Mn^{7+} to Mn^{4+} in solution with low pH by agents like ethanol in acetonitrile and oxidising Mn^{2+} to MnO_2 by agents like BrO_3^{-} and $S_2O_8^{2-}$ [19]. By altering the pH various products such as Mn_3O_4, β-MnOOH and γ-MnOOH can also be obtained [19, 31].

S. Pang et al [24] discovered another useful and effective approach to synthesise α-MnO_2 is using Mn^{2+} to reduce MnO_4^{-}, e.g adding $MnSO_4$ into $KMnO_4$ solution or mixing $KMnO_4$ with manganese (II) acetate solutions in water. Such reactions are generalized in equation (2.3) [19].

$$2MnO_4^{-} + 3Mn^{2+} + H_2O \leftrightarrow 5MnO_2 + 4H^+ \qquad (2.3)$$

$$4KMnO_4 + 3C + 2H_2SO_4 \leftrightarrow 4MnO_2 + 3CO_2 + 2K_2SO_4 + 2H_2O \qquad (2.4)$$

It is worth mentioning that MnO_4^{-} can be reduced by carbon and forms a uniform coating MnO_2 onto, e.g the surface of a graphite electrode through one step reaction in an acidic solution [31], as in equation (2.4). This inspiring discovery suggested a simple route in synthesising various MnO_2/Carbon composites, including carbon nanotubes (CNTs), activated carbon materials and exfoliated graphite plates.

2.4.2 Electrochemical Synthesis

A prominent advantage of synthesizing MnO_2 through electrochemical deposition is that the product will be in form of a homogenous thin film on a conducting substrate, i.e. graphite, stainless steel, titanium foil, etc., without using any binder. This can largely improve the situation of a resistive electrode caused by the aggregation of manganese oxide powders. The reaction of electrochemical deposition is represented in the below equation [19].

$$Mn^{2+} + 2H_2O \leftrightarrow MnO_2 + 2e^- \tag{2.5}$$

Successful electrochemicals depositions have been carried out with various precursors, including manganese acetate, manganese sulphate, manganese chloride, etc.; manganese acetate was claimed to be a superior precursor among all due to its high deposition rate at much lower potentials and the existence of acetates having offered a more controllable reduction in the deposition material. However the capacitance performance is independent of precursors as the mean oxidation state of Mn is not significantly affected by changing anions of manganese precursors. Different electrodepositing conditions, galavanostatic, potentiostatic and potentio-dynamic were compared and the potentiodynamic deposition was claimed to be able to produce superior MnO_2 with optimum capacitive behaviour [32, 33].

The deposition conditions and the deposition potential have been proven to have profound influence on the oxidation state of the manganese, the nanostructures, BET surface area and eventually electrochemical performance of the product. On average the specific capacitance of the MnO_2 synthesised from electrochemical deposition is slightly above 200F/g, with the thickness of the film is of several tens of nanometre.

However, the figure could drop drastically as the thickness increases according to J. Broughton et al [34].

J. Broughton et al [34] made another interesting finding that electrochemical oxidation can be an effective method to convert non-capacitive manganese metallic compound and crystalline oxide Mn_3O_4 into capacitive MnO_2. The transformed MnO_2 was confirmed to be the layer structured birnessite. High capacitance of 600-700F/g was reported for 20 nm thin films with a low current density of 160 µA cm^{-2}. A high scan rate of 500 mV s^{-1} was achieved, resulting in a capacitance of 170 F g^{-1}. An obvious advantage of this discovery is that it separated the coating process from the activation process, thus convenient techniques like sputtering and electrostatic spray can be employed to produce homogenous thin film at large quantity with low cost. However, for thin films synthesised in this manner, the thickness, corresponding to the electrolyte accessibility, remained a limiting factor for the capacitance and the maximum achievable capacitance reaches was 50 F g^{-1}.

2.4.3 Sol-gel route

Sol-gel route is based on the hydrolysis and condensation of manganese ions. It was developed with the aim of producing colloidal sols containing nanoparticles which can be deposited as very thin porous films on a substrate via dipping or spinning procedure [35]. It has been discovered that homogenous and highly porous MnO_2 powders can be synthesised through this route.

J. Xu et al [35] reduced Mn^{7+} into amorphous MnO_2 by fumaric acid as represented in the below equation (2.6)

$$3C_4H_4O_4 + 10KMnO_4 \leftrightarrow 10MnO_2 + 3K_2C_2O_4 + 4H_2O + 4KOH + 6CO_2 \qquad (2.6)$$

Drying of the MnO_2 gel at room temperature can produce densified xerogel of MnO_2. However, xerogel has exhibited less satisfying capacitive behaviour compared with porous hydrous MnO_2 films and underwent severe capacity loss of 50% after eight charge-discharge cycles.

It is also reported that a stable colloidal MnO_2, with a high concentration of MnO_2, can be prepared by reduction of tetraalkylammonium (methyl, ethyl, propyl and butyl) permanganate salts in aqueous solutions with 2-butanol and ethanol. This sol-gel derived tetrapro-pyammonium MnO_2 thin film on nickel substrates exhibited good electrochemical behaviour [19].
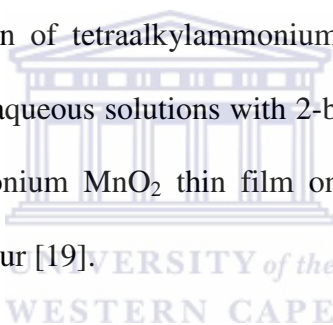
2.5 Important Parameters Influencing Pseudo-Capacitive Performance

2.5.1 Electrode Property and Treatment

2.5.1.1 Crystalline Structure

In nature, MnO_2 have a number of polymorphs with many types of tunnel and layered structures. The XRD pattern of several commonly occurred MnO_2 are represented in figure 2.2. Crystalline structures have been found to have profound impacts on the electrochemical performance of the MnO_2 by transforming distorted spinel Mn_3O_4 to layered structure birnessite through potential cycling in aqueous

Na_2SO_4, an increased capacitance of more than 20 times the value of the original spinel Mn_3O_4. Early researchers, however, showed more interest in amorphous MnO_2 and nanocrystalline compounds for the application in electrochemical capacitors, with the belief that the porous morphology can enhance the ion accessibility and cation diffusion. Nevertheless, the poorly crystallised MnO_2 contains intergrowth of different tunnel structures, leading to more difficult cation diffusion and resulting in higher resistance . The maximum capacitance of this type of material is limited by the upper limit of BET surface area it can be achieved [36, 37, 38, 39].
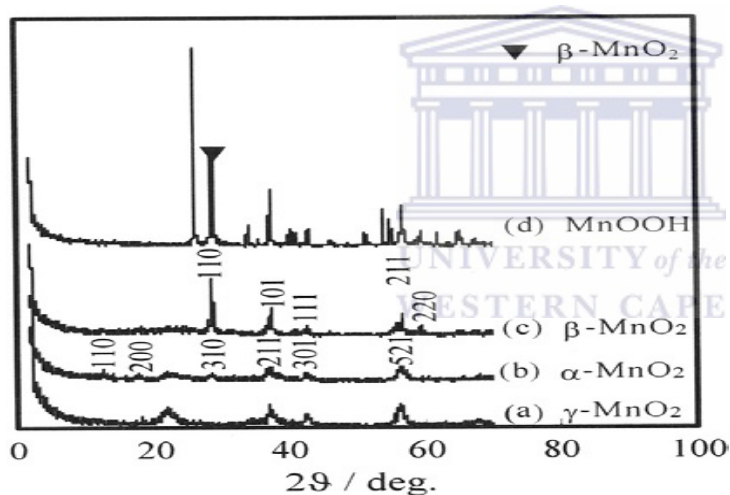
Figure 2.2: *Patterns (XRD) of α-MnO₂, β-MnO₂ and γ-MnO₂ [19]*

M Toupin et al [39] have recently made several attempts to explore the crystallised MnO_2 material. Various types of MnO_2 including α-MnO_2, β-MnO_2, γ-MnO_2 and δ-MnO_2, with one dimensional and 3 dimensional tunnel structures, and birnessite ζ – MnO_2 with layered structures, has been tested for possible application as the cathode material. It was reported that for MnO_2 with various crystalline structures, the birnessite materials doped with potassium with two-dimensional structure is at adventure as the presence of K^+ ions inside the two dimensional tunnels allow the

participation of a larger fraction of the MnO_2 to the charge storage process; while the specific capacitance of the materials with one dimensional tunnel structures is generally low, e.g. γ-MnO_2 of 30 F g^{-1} and β-MnO_2 merely 5 F g^{-1}, because of slow cation diffusion which limited the charge storage processes to the surface.

A more fundamental reason is that the structure change also leads to significant change in conductivity, which eventually influences the pseudocapacitive behaviour. Owing to the Jan-Teller distortion of the $Mn(III)O_6$ octahedron, the conductivity of MnO_2 involving trivalent Mn (III) is rather low as compared to that of MnO_2 or amorphous manganese (oxyhydro)- oxides involving Mn (IV) [40]. When transforming thermodynamically stable γ-Mn_2O_3 into α-Mn_2O_3 and Mn_3O_4 by mechanical grinding [40], it was discovered that the capacitance of MnO_2 decreased linearly with decreasing crystallinity of γ-MnO_2 due to the formation of $Mn (III)O_6$ octahedron [40].

Thus, it can be concluded that although the majority attention is still focussed on the study of the amorphous MnO_2, crystalline MnO_2 with suitable tunnelled structures represents a group of rising candidates for the electrode materials for the supercapacitors.

2.5.1.2 BET Surface Area and Pore Size

In general, larger surface area indicates higher accessibility of the active material, leading to a better capacitive behaviour. Several research projects focusing on synthesising MnO_2 with larger effective surface area have yielded encouraging

results [41, 42]. Efforts have been made to enhance the surface area and porosity of MnO_2 films by adding surfactant, sodium lauryl sulphate and triton X-100 during electrodeposition [41]. Enhanced surface area of 76.4 and 84.46 $m^2 \, g^{-2}$ were reported with the addition of these two surfactants respectively, corresponding to 20 and 60% of improvement in specific capacitance. On the other hand, a fade of 40% in capacitance has been reported due to a 50% decrease in surface area from the ageing of the coprecipitated MnO_2 [39].

However, it was suggested that for amorphous MnO_2, the capacitance reaches a maximum at a surface area of 200 $m^2 \, g^{-1}$, further increase in the surface area does not provide additional charge storage [39]. Moreover, it was claimed that specific capacitance depends on the pore size distribution rather than BET surface area. Since the function of the pore size and pore structure on the double layer capacitive process have been well studied [19], it is worthwhile to extend the research into the process of pseudo-capacitance.

Based on the transmission line model mathematical models considering the effect of the pore size distribution for the impedance of porous materials have been developed with various research findings to complement the understanding [43, 44]. It was observed for the two types of MnO_2, in the forms of xerogel and ambigel, with similar surface areas of 63 and 72m^2g^{-1} respectively, the xerogel only exhibits 56% of the capacitance ambigel. As the majority of the pore diameters of xerogel are < 20nm, while ambigel are mesopores with diameters of 20-100nm. Similar conclusion that a higher percentage of large pores can ensure the delivery of higher power at higher charge/ discharge rate was also drawn from the MnO_2 film synthesised by

potentiostatic deposition. Moreover, three types of porous MnO_2, ordered mesoporous β-MnO_2 with [1 x 1] channels, disordered mesoporous γ-MnO_2 with [1 x 2] and [1 x 1] channels and disordered porous α-MnO_2 with [1 x 1] and [2 x 2] channels, were synthesised to study the relationship between electrochemical properties and pore structure MnO_2.

It was declared that the capacitance profiles of the three types of one-dimensional tunnel structure MnO_2 are clearly dependent upon the pore structure despite of their crystalline structures. Mesoporous, especially ordered mesoporous MnO_2 has superior capacitive performance rate capability and high performance in 1M Na_2SO_4 solution due to its lower pore resistance and its better accessibility of ions to the electrochemically active surface [19].
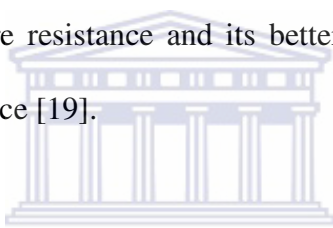
Thus, it is to conclude that surface area as well as the pore structure is the determinant factors for the accessibility of the MnO_2 to the electrolyte, which limits the depth and rate of ions transfer within the bulk materials. Engineering MnO_2 with desirable structure of organised mesopores and macropores may enhance the overall capacitive performance.

2.5.1.3 Thickness and loading of manganese dioxide

Thickness is a key limiting factor for the capacitive performance of MnO_2 materials. Significant decrease in specific capacitance with increasing electrode thickness has been reported by most research groups, disregarding whether the material was synthesised by electrodeposition, sol-gel route or chemical deposition.

Often, exceedingly low loading of the MnO_2 was applied onto the electrode to ensure a 'high specific capacitance' on the order of tens of mg per cm^2 [41, 42], or with a thickness of tens of nanometres. S. Devaraj *Et al* [41] proved with the loading of 0.03mg cm^{-2}, even an extreme high capacitance of 1330 F g^{-1} would only provide an electrode capacitance of 0.039F/cm^2, which is of little use for real world application with high power and energy demand. Even at loading, the decreases in specific capacitance with increasing the loading are discernable. A 55% decrease in its initial specific capacitance of 330 F g^{-1} was reported when the loading was increased from 18 to 116 µg cm^{-2} for the thin layer of MnO_2 obtained from electrostatic spray deposition [38]; similar observations were made with MnO_2 obtained from chemical deposition and electrodeposition [34].

Essentially, this limiting effect of the thickness of the MnO_2 loading is the combined results of the low electrical conductivity of MnO_2, the obstruction from the longer path for the diffusion of protons and other ions [35]. T. Brousse *Et al* [39] also suggested that only a limited fraction of the MnO_2 composite is electrochemically active. No change of the manganese oxidation state was detected for the inner layer of the thicker film electrode, a finding totally different from the case of thin film electrode. Besides, the specific capacitance obtained so far are still far from theoretical value of more than 1000 F g^{-1} which implies the existence of a vast amount of material that has not been utilised.

However, amelioration has been proved effective in improving the situation. For example, introducing CNTs into the MnO_2 during synthesis can form a 3D porous and conducting network of CNTs to assist the electron and ion transfer within the MnO_2. An electrode capacitance of 5 F cm^{-2} at high loading of 35 mg cm^{-2} was

achieved in this manner. Various attempts to overcome the limitations of the thickness have been made, many of which have achieved encouraging results [41, 45].

2.5.1.4 Annealing Temperature

A number of studies have been carried out about the effects of annealing temperature and annealing time on the electrochemical activity of MnO_2. Essentially, annealing treatment results in three transformations in the manganese oxides: loss of water content, decrease in surface area and changes in structure. The effects of annealing on these aspects will be discussed in detail.

Water content in MnO_2 is known to affect the electrochemical reactivity and thermodynamics stability of various MnO_2 phrases as it causes a variation in crystal lattice and a consequent variation in electrical conductivity and electrode potential [24]. Heat treatment as a temperature up to $200^{o}C$ is believed to remove physically and chemically adsorbed water molecules [25]. The loss of water molecules means a reduced weight, which may lead to a small increase in specific capacitance; however, it also leads to a decrease in surface area, which can vitally hinder the electrochemical activity [25, 46]. Furthermore, chemically bound water is believed to be essential for the transportation of active ion species. Consequently, the loss of water content through heat treatment will lead to the loss of pseudocapacitance. The increases in water content leads to increase in ionic transport while the decrease in electronic transport at the same time. Thus, heat treatment up to a certain level can possibly enhance the overall pseudocapacitive behaviour, although most researchers

observed monotomic decrease in specific capacitance upon heat treatment even at temperatures below 200°C [25, 46-49].

Significant structure changes, together with a drastic decrease in surface area, will occur at an annealing temperature above 300°C [19]. As described in the section on 'Crystalline structure', certain crystalline structures of MnO_2 are less favourable for the charge storage mechanism; transition into one of these crystalline structures will definitely diminish the pseudocapacitance of the electrode material. The transformation from amorphous and hydrous MnO_2 to Mn_3O_4 and Mn_2O_3 with crystalline structures was observed upon the increase in annealing temperature up to 600°C. Condensation, rearrangement, reconstruction and growth of the deposited MnO_2 as a function of temperature were recognized by atomic force microscopy during annealing. It was concluded that heat treatment at temperature higher than 200°C will promote the formation of crystalline Mn_3O_4 and Mn_2O_3 and consequently result in the loss of pseudo-capacitive properties of the oxides.

S. Devaraj *Et al* [46] reported the corresponding decrease in BET surface area upon the transition from α-MnO_2 to Mn_2O_3 through annealing from 70°C to 800°C. Deterioration of α-MnO_2 with tetragonal unit cell structure was observed with increasing annealing temperature, especially at temperatures higher than 300°C, and a continuous decrease in BET surface area, from initially 190 to 145 m^2 g^{-1} at 300°C and finally 8 m^2 g^{-1} for the Mn_2O_3 annealed at 600°C and above, was attributed to agglomeration of particles on annealing. The corresponding degradation in capacitive performance was observed, with a loss of 13% of its specific capacitance upon annealing at 200°C [74], due to the loss of water content, and a further drastic

63% loss at the annealing temperature above 400°C, due to the transition from α-MnO$_2$ to Mn$_2$O$_3$.

2.5.2 Electrolyte

The choice of electrolyte also has significant impacts on the performance of the MnO$_2$ electrodes. The pH condition is an important determinant of operating potential window; and different existing ions determine the rate of intercalation and the situation of corrosion. Thus, desirable electrode performance can be obtained by choosing the electrolyte carefully.

2.5.2.1 pH Conditions

Electrochemical reversibility and the charge storage mechanism of hydrous MnO$_2$ largely depend on the pH of the electrolyte. Because Mn(II) and Mn(VII) are soluble in the electrolytic solution, the reaction of Mn (IV) to Mn (II) and Mn (IV) to Mn (VII) should be avoided during charging and discharging the capacitor [45].These irreversible reactions will lead to partial dissolution of the electrode and subsequent decrease in capacitance and cycling reversibility [45].

On the other hand S.H. Lee *Et al* [50] suggested that the pH condition affects the water decomposition and gas evolution, which also limits the operating potential window. Gas evolution reactions are related to H$_2$O decomposition, H$^+$ reduction and OH$^-$ oxidation, the presence of excessive H$^+$ ions induces H$_2$ gas evolution at -0.2 V, which limits the operating voltage to approximately 1.2V, while the presence of excessive OH$^-$ ions results in O$_2$ gas evolution at 0.7V by their oxidation process,

limiting the operating voltage window to 1.8V. An operating voltage window of 2V was achieved with the 1mol/L KCl electrolyte in which the electrode reaction for H_2O decomposition were observed at potentials of 1.1V (anode) and -0.9V (cathode), (Ag/AgCl reference electrode) [50]. The negative shift of the cathode reaction potential was likely to be responsible for the increased cell voltage (2.0V) as the result of a high overpotential for the hydrogen evolution reaction as in the below equations.

$$2H_2O \leftrightarrow O_2\,(g) + 4H^+ + 4e^- \qquad\qquad (2.7a)$$

$$4OH^- \leftrightarrow O_2\,(g) + 2H_2O + 4e^- \qquad\qquad (2.7b)$$

$$2H^+ + 2e^- \leftrightarrow H_2\,(g) \qquad\qquad (2.7c)$$

$$2H_2O + 2e^- \leftrightarrow H_2\,(g) + 2OH^- \qquad\qquad (2.7d)$$

2.5.2.2 Ion Size and intercalation

It was reported that electrolyte with equal transference numbers for both cation and anion can promote capacitive behavior and anions with smaller hydration sphere and smaller size leads to faster diffusion and higher chemisorptions rate [51]. Experiments comparing the electrochemical performance of the MnO_2 material in several neutral aqueous electrolytes including NaCl, KCl and LiCl with the same concentration of 2mol/L have been conducted [19, 51]. It was claimed that although Li^+ is smaller than Na^+ and K^+, it has a larger hydration sphere, which makes it disadvantageous. And this theory supported by the results from several other research groups.

However, a more recent study by A. Yuan et al [52] on the electrochemical behavior of the MnO_2 electrode in 1 mol/L KOH and 1 mol/L LiOH declared that the reaction mechanism of MnO_2 electrode in LiOH appears to be Li^+ ion insertion/extraction in the MnO_2 solid, followed the battery reaction of $MnO_2 + xLi^+ + xe^- \leftrightarrow Li_xMnO_2$. This finding may elicit further thoughts upon the mechanism of the charge storage within MnO_2.

2.5.2.3 Corrosion and non-aqueous electrolytes

Another major concern in selecting electrolyte is the issue of corrosion. Although chloride solutions normally have higher ionic conductivity which is desirable, they are likely to cause corrosion on stainless steel current collector. Thus platinum or titanium current collectors are normally applied in chloride electrolytes. On the other hand, sulphate based salts, although with lower ionic conductivity and lower solubility, showed long term cycling stability with stainless steel current collector. This trade-off between ionic conductivity and corrosion resistance is thus up to the individual researchers to decide [19].

Alternatively, using an organic solvent provides a solution for the corrosion issue. J. Jiang et al [53] tested the electrochemical performance of electrochemically deposited MnO_2 in degassed acetonitrile solution containing 0.1mol/L $TBAClO_4$ (TBA= tetrabutylammonium) and 0.2mol/L H_2O was studied. A 2V potential window was achieved; the presence of water in the organic solvents facilitates the capacitive behaviour, yet limits the potential window. However, the higher resistance of the organic solvent impedes the capacitive performance of the electrodes [53].

The specific capacitance calculated from organic solution is only 60% of that from aqueous solutions. Furthermore, a gel electrolyte of aqueous solution of KCl in potassium poly (-acrylate) polymer with ionic conductivity in the order of 10^{-1} s cm^{-1} was proposed to be used in the $MnO_2.nH_2O$ supercapacitor [54]. It was reported that the polymer component did not impose a negative effect on leakage current and the supercapacitor with the gel electrolyte in fact delivered substantially higher specific capacitance than those in the liquid electrolyte with the same salt (KCl) composition (1mol dm^{-3}). This improvement was attributed to the hydrophobic nature of the polymeric component in the gel, which enhanced the compatibility between the electrode matrix and the electrolyte, and essentially increased the wettability. On the other hand, the swelling process of the polymer molecules within the electrode interior can open closed pores which increased the electrolyte accessibility [54].

2.5.3 Separator

The separator is the major contributor to the resistance of the MnO_2-based SCs. Consequently the separator is a major factor dictating the power density of MnO_2-based supercapacitors. The membranes that are used commercially as separators are created from a range of polymeric materials. When the separator is wetted with the electrolyte, there are five structural features that can be identified as having possible effect on the resultant SC. The features are tortuosity, porosity, pore size, pore size distribution and thickness. Commercial polymeric separators are generally manufactured by employing extrusion and orientating process step. These processes invariably produce a separator that is effectively many-inter tangled polymer strands with void space between the strands. Resistance is the measure of freedom of ionic and electronic movement through a media. In this context a electronic movement

occurs through the current collectors, the binder and the MnO_2 electrodes. Ionic movement occurs through the electrolyte that is imbibed into separator pores [16].
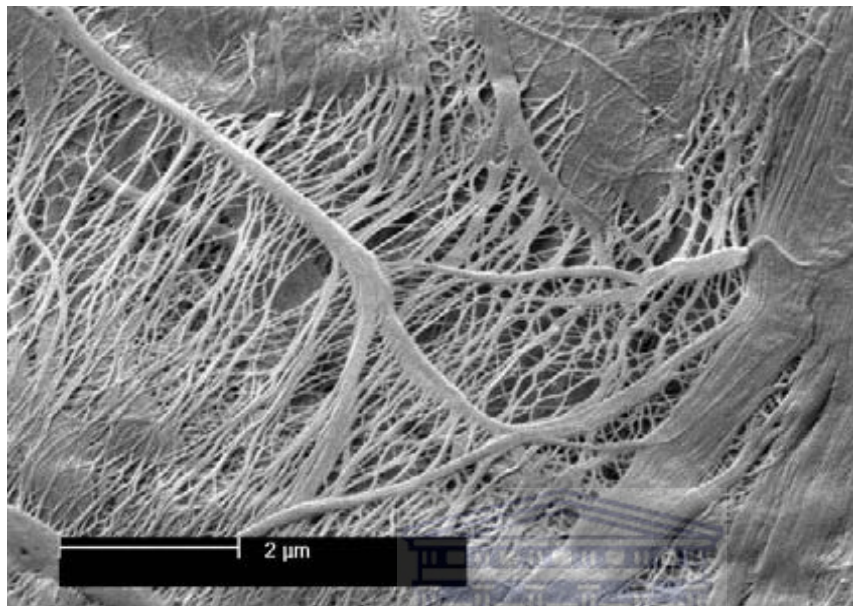
Figure 2.3: *SEM image of commercial separator polytetrafluoroethylene [16]*

2.6 Cell performance

Although extensive studies have been conducted in the synthesis and characterisation of MnO_2 for the application as an electrode material for supercapacitors, very few of them were extended to the characterization of cell performance, partly because the low loading of MnO_2 may result in disappointing cell capacitance and power characteristics.

2.6.1 Symmetric cell

Traditionally, electrochemical capacitors have a symmetric structure, especially for those made of carbon materials with high surface areas. The total cell capacitance is determined by the electrode with a smaller value of the capacitance (equation 2.8).

Therefore, the maximum cell capacitance is to be achieved when the two electrodes have identical capacitance.

$$\frac{1}{C_{cell}} = \frac{1}{C_{positive}} + \frac{1}{C_{negative}}$$ (2.8)

In addition, energy density and power density, which can be derived from equations (2.9) and (2.10) respectively, are two widely used characterisations for supercapacitors for their real world applications. It is worth pointing out that that energy and power densities are both related with the cell voltage and can only be meaningful for a cell or a stack of multiple cells. They should not be used to describe individual electrode materials [19].

$$E = \frac{1}{2}C_m V^2$$ (2.9)

$$P = VI_{max}$$ (2.10)

Where C_m is the mass specific capacitance and V is the operating potential window.
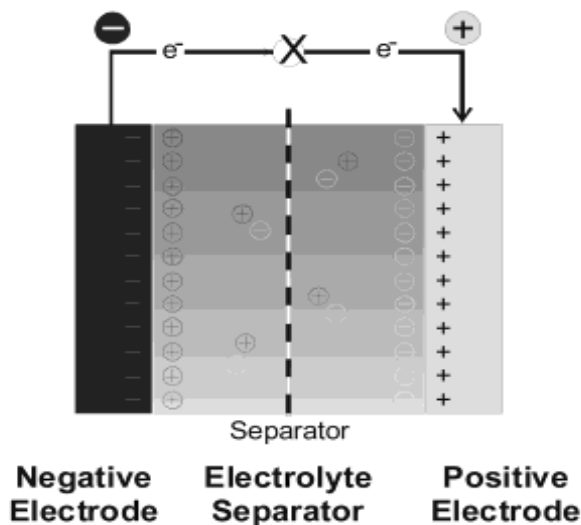
Figure 2.4: *Representation of a supercapacitor, illustrating the energy storage [15].*

F. Beguin *Et al* [45] fabricated two symmetrical electrode cells with MnO_2 respectively. Interestingly, it was found out that the two identical electrodes of the symmetric cell, however, work in different potential range, namely, after charging the cell to 0.6V, the polarisation of the negative electrode (E= 0.32V) is larger than the polarisation of the positive electrode (E= 0.28V). In a cell configuration like this, the limited operating potential window is a major drawback, as a small operating potential window affects the energy and power performance directly (equations 2.9 and 2.10). Moreover, the electrochemical stability is a fundamental issue. The negative electrode of the symmetric cell was reported to operate in the range of an irreversible Mn (IV) to Mn (II) reaction, which results in the dissolution of the electrode and consequently, poor cycling stability [55].

2.6.2 Hybrid Cell

Owing to the disadvantages of the symmetric cells, hybrid cells employing asymmetric electrodes with different operating voltage windows were proposed [50]. A prominent advantage of the hybrid cell system is the enlarged operating potential window, which noticeably enhances the energy and power performance (equations 5 and 6). In aqueous systems, this is of particular interest as it may allow the capacitor to be operated at a potential window wider than the water decomposition voltage of 1.2V, if electrode materials with high overpotentials for hydrogen or oxygen evolutions are carefully selected. One particular issue with hybrid supercapacitors is non-linear charge-discharge, nevertheless promising results from various research groups indicated that this can be avoided by appropriate cell fabrication [56].
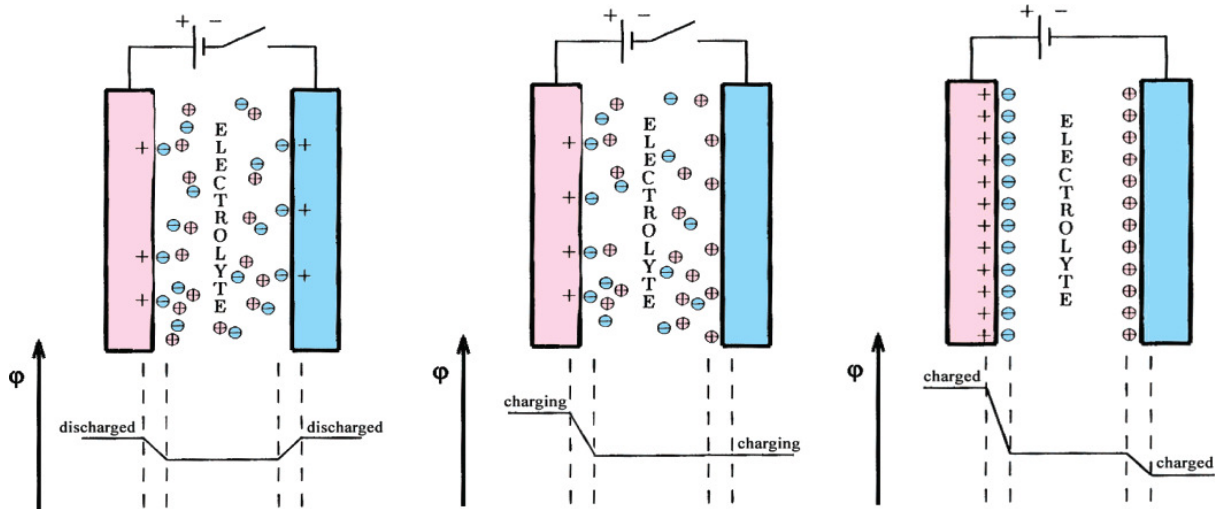
Figure 2.5: *Depiction of a charging process of asymmetric capacitor [15].*

2.6.2.1 With carbon materials

The relatively low electrical conductivity of MnO_2 limits its loading and thickness as an electrode material, which eventually limits the energy density of the electrode and hinders its applications in supercapacitors. Various methods have been developed to overcome this shortcoming and the introduction of carbon materials has been proven to be an effective method to increase the conductivity. Different carbon materials, e.g. carbon black, acetylene black, CNT and exfoliated graphite, have been employed to form composites with MnO_2 with the aim of promoting conductivity and boost the utilisation of the redox capacity of MnO_2 [53, 56].

Carbon materials, with their well known advantages of high potential for hydrogen evolution, good double layer capacitive behaviour, excellent cycling stability and electrical conductivity are undoubtedly a favourable choice for the MnO_2 asymmetric cell. Hybrid supercapacitors with MnO_2 as the cathode and carbon

materials such as activated carbon [50, 52] and multiwalled CNTs as the anode have been fabricated.

Carbon nanotubes is another favourite choice (fig 2.6); the unique tubular structure is believed to be able to produce consistent composites and an interconnected conducting network with high porosity for enhanced electron transfers well as electrolyte accessibility [19]. Although enhanced capacitive performance was reported for composites synthesised with both multiwall CNTs and Single wall CNTs [57] multiwall CNTs are more favourable one. It was claimed that compared with carbon black, CNTs are more a more effective additive in enhancing conductivity of MnO_2. The average specific capacitance of the MnO_2/CNT composites is expected to be in the range of 110-568 F g^{-1} [58] depending on the electrode fabrication
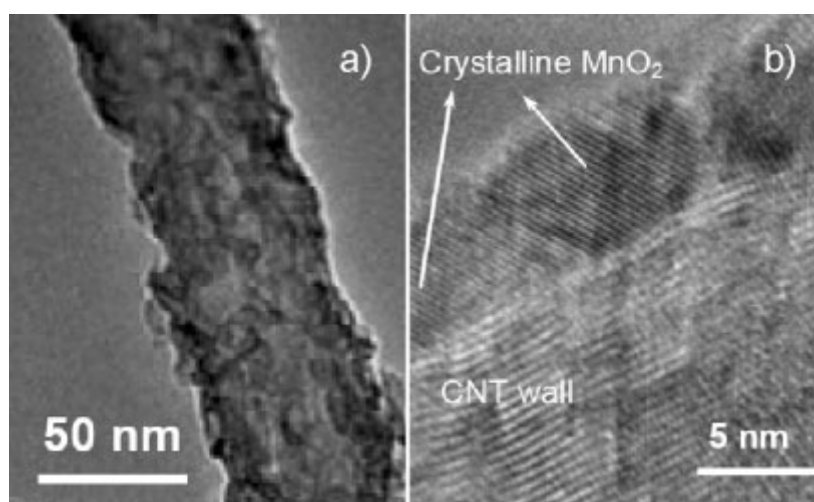
Figure 2.6*: Image (TEM) of MnO₂/CNT composites* [19].

These hybrid systems exhibited superior capacitive behaviour in comparison with the symmetrical MnO_2 systems. Operating potential windows at or larger than 10V

(fig 2.7a) were realised in most cases [50]. Although it was pointed out that by narrowing the operating potential window to 1.5V, a better cycling stability can be achieved M. Toupin *Et al* [59] since the reduction of Mn^{4+} to soluble Mn^{2+} species, and hydrogen and/or oxygen evolution occurred when the hybrid cell was cycled over an operating potential window of 2.2V [59]. However, a 24% decrease in the initial energy density was still observed with this hybrid cell after 23000 cycles tested between 0 and 1.5V in 0.65 mol/L K_2SO_4 [59], which was believed to be caused by the ions being trapped in the MnO_2 electrode, blocking the active sites, rather than the dissolution of the Mn (IV).
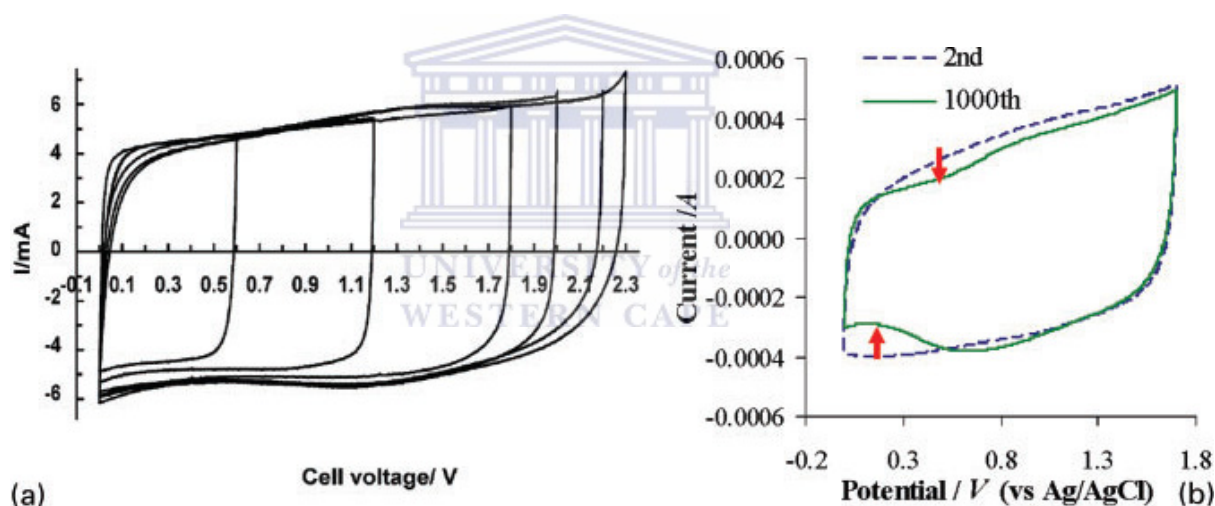
Fig 2.7: a MnO₂ and activate carbon in 2 mol/l KNO₃. b CNT/SnO₂ vs CNT/MnO₂ in 2mol KCl [19].

2.6.2.2 Loading with other active Materials.

Metal oxides including Fe_3O_4 $LiMnO_4$ [147] and SnO_2 were examined as the counter electrode materials from the hybrid cells. The Fe_3O_4/MnO_2 cell exhibited an operating potential window of 1.8V in the aqueous solution, although the cell

performance was later described to be inferior to the MnO_2/carbon cell [19, 58]. It provided a cheaper alternative to activated carbon.

A semi-battery structure with MnO_2/CNT and $LiMn_2O_4$ as electrodes was characterised in 1mol/L $LiClO_4$ in polycarbonate, with specific energy of 56 Joules and a apecific power of 300 watts. It is worth mentioning that in a hybrid cell of SnO_2/MnO_2, the MnO_2/CNTs composite was explored as the anode material, different from the common understanding that MnO_2 is a type of cathode material. An operating potential window of 1.7V (figure 2.6b) was achieved in aqueous electrolytes, and an energy density of 20.3 joules was obtained at the current density of 0.25 A g^{-1} with only 8% loss of its capacitance after 1000 cycles [58].

Conducting polymers, including PAni, PPy and PEDOT, have been respectively fabricated into hybrid supercapacitors with MnO_2 [55]. Compared with the MnO_2/carbon hybrid cell; the MnO_2/conducting polymer cell exhibit higher capacitance but narrower operating potential windows in aqueous solutions: 1.2, 1.4 and 1.8V for α-MnO_2/PAni, α-MnO_2/PPy and α-MnO_2/PEDOT respectively [60]. These figures are still considerably higher than symmetric MnO_2 cell.

2.7 Conclusion

Based on previous reports, the key factors that dictate the selection of electrode materials for supercapacitors are the following: (1) high specific surface area, leading to the large capacitance; (2) Suitable surface functional groups to enhance the capacitance by additional faradaic redox reaction and improve the wettability; (3) large pore size and short pore length to facilitate the ions diffusion with a high speed;

(4) low internal electrical resistance, which leads to fast charging-discharging; (5) low volume and weight; (6) low price; (7) environmental friendly materials; (8) thinner electrodes and current collectors [61].

Recent research progresses in relation to manganese oxide for supercapacitor application have been critically reviewed. The pseudocapacitance of MnO_2 is faradaic in nature and has been qualitatively explained according to the band theory for semiconductors. Emphasis has been given to the synthesis and the electrochemical behaviour, particularly charge storage in various forms of pure on composited MnO_2. Important parameters that can influence the electrochemical behaviour of MnO_2 based materials are summarised. Appropriate cell configuration has been proven to be the necessity for the optimisation of the capacitive performance of MnO_2 based supercapacitors [19].
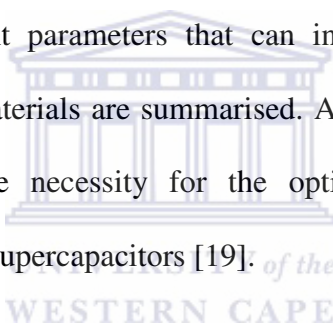
Based on these literature findings, the author believes the MnO_2 represent a promise and very competitive electrode material for application in supercapacitor.

Chapter 3: Experimental Method

MnO_2 is a promising SC material due to the low cost of the raw materials and the fact that manganese is considered more environmental friendly than other transition metal systems. These compounds show high specific capacitance varying between $100Fg^{-1}$ and $300Fg^{-1}$ and a good cyclability. The synthesis of MnO_2 electrodes was conducted under different conditions, by using different synthetic routes. MnO_2 with different chemical and physical properties has previously been synthesised by simple reduction, coprecipitation, thermal decomposition, electro-deposition and sol-gel processes.

MnO_2 have structural flexibility and can appear in different crystallographic polymorphs such as α-, β-, γ-, δ- and ε-MnO_2 [18]. The large number of structure types that exists in the MnO_2 system is attractive from the point of view that it offers a wide selection of different materials based on one compound [62]. Consequently, rational synthesis of MnO_2 materials with controllable crystal structure, morphologies and size is very important [18].

In this chapter various methods that were used for synthesising of the oxide are discussed in details. The physiophysical characterization of the optimised by-products procedures are discussed as well as the electrochemical characterizations. Different parameter that affects the capacitance will be discussed, and how some problems were overcame. Each and every chapter will begin with a brief background and introduction of the detailed methodology.

3.1 Chemicals and Apparatus

Chemicals used for the preparation of metal oxide and the preparation of electrode are given in table 3.1 and 3.2 respectively.

Table 3.1: Chemicals used for the preparation of metal oxide

Chemical	Supplier (location)
$KMnO_4$	Merck (Cape town)
$MnCl_2.4H_2O$	Merck (Cape town)
$MnSO_4.4H_2O$	Merck (Cape town)
$(NH_4)_2SO_4$	Merck (Cape town)
$(NH_4)_2S_2O_8$	Industrial analytical (Kyalami)

Table 3.2: Chemicals used for the preparation of the electrode

Chemicals	Supplier (Location)
NMP	SAIAMC
PVDF	SAIAMC
Carbon Black	SAIAMC
Potassium hydroxide	Industrial analytical pty ltd(Kyalami SA)
Sodium Sulphate	Industrial analytical pty ltd (Kyalami SA)
Carbon Paper	SAIAMC

SAIAMC = South African Institute for Advanced Material Chemistry

N.B. All water was tapped from Milli-Q® ultrapure water system with a resistance of 18.3 MΩ. cm.

3.2 Synthesis of the metal oxide

MnO_2 with different chemical and physical properties can be prepared under different synthesis conditions. Many routes for the preparation of MnO_2 have been developed including simple reduction, coprecipitation, thermal decomposition, electrodeposition, sol-gel processes. Subramanian [63] prepared MnO_2 by the reduction of $KMnO_4$ with $MnSO_4$ under hydrothermal conditions, Reddy and Reddy [64] reported the synthesis of ambigel MnO_2 and xerogel MnO_2 by the sol gel method. Xu [65] synthesised α-MnO_2 hollow spheres and hollow urchins by the hydrothermal decomposition of $KMnO_4$ with H_2SO_4 solution. Lee and Goodenough [66] have synthesised MnO_2 by the co-precipitation involving $KMnO_4$ and manganese acetate. Xue [67] prepared mesoporous MnO_2 by electrodeposition method in a triblock copolymer template. Raguthapy [68] used aniline to reduce $KMnO_4$ at room temperature to obtain amorphous MnO_2, which would be converted to crystalline α-MnO_2 at higher temperature.

3.2.1 Synthesis of MnO₂ electrode via the Reduction method under low temperature (LT) conditions.

All the chemical reagents were of analytic pure grade and used as received. $KMnO_4$ and $MnCl.2H_2O$ were grinded in a glass mortar under room temperature in the fume cupboard at ratio of 2:3 at room temperature; the reagents were grinded for 30 minutes. The resultant mixture was transferred into a vial and was heated in a water

bath at 70°C. The reaction has been varied from 1 to 6 hours in order to optimise the synthesis conditions. The as-prepared products were filtered, washed with distilled water for several times, and vacuum dried at 100°C for three hours.

3.2.2 Co-precipitation method under Hydrothermal (HT) conditions.

$(NH_4)_2SO_4$, $MnSO_4.4H_2O$ and $(NH_4)_2S_2O_8$ were dissolved in 40mL of distilled water under stirring conditions with a ratio of 1:2:2, the solution was transferred in 100mL volumetric flask and distilled water was added to make 0.1L solution. The resultant solution was transferred into six Teflon-lined autoclaves and held at 120°C in the furnace for different times. The reaction time was also varied from 1 to 12 hours in order to optimise the synthesis condition. The Autoclaves were taken out and cooled down to room temperature naturally. The as-prepared product was filtered, washed with distilled water for several times, and vacuum dried in the oven for overnight at 120°C.

3.3 Physiochemical Characterization of the metal oxide

A whole range of physical characterization techniques can be used to study the nanostructures of the MnO_2 electrodes. The effect of varying the reaction time to synthesise the MnO_2 nanostructures and forming mechanism of α-MnO_2 nanorods will be investigated by the following techniques:

- ➢ X-ray diffraction (XRD)

- ➢ Scanning electron Microscopy (SEM)

- ➢ Electron dispersive Spectroscopy (EDS)

> ➤ Transmission Electron Microscopy (TEM)

> ➤ N_2 Adsorption-desorption

3.3.1 X-ray diffraction

XRD is the only method that permits the direct identification of any crystalline material based on their unique crystal structure. Such materials include minerals, metals, alloys, semiconductors, polycrystalline materials, superconductors, polymers, textile fibers, gemstones, proteins, as well as any other synthetic inorganic and organic crystals. XRD can also measure qualitative and quantitative phase analysis. The metal surface area of MnO_2 could be determined using particle sizes obtained via XRD. Crystalline structures have been found to have profound impacts on the electrochemical performance of the MnO_2. XRD was solely used to determine the crystal structure and particle size of the electrode. The Scherrer equation (eq 3.1) was used to determine the average particle size of the MnO_2.

$$D = 0.9\lambda/\beta \cos\theta \tag{3.1}$$

Where D is the mean size of the crystals, 0.9 is the shape factor, λ is the x-ray wavelength, β is the line broadening at half maximum intensity in radians and θ is the Bragg angle.

These are the parameters and equipments that were used for XRD analysis:

X-ray diffractometer: D8 Advance Bruker AXS

 X-ray source: Copper tube with Cu K_α ($\lambda = 1.5406$ Å)

Detectors: PSD Vantec-1, Gas detector with 1600 channels

Generator Operation: 40kV and 40mA

Variable slits: V20

2$\square$ Range: 5 - 100

Scan rate: 0.028

Measurement time: 2 sec/step

3.3.2 Scanning Electron Microscopy

Scanning electron microscopy (SEM) is a type of electron microscope that images the sample surface by scanning it with a high-energy beam of electrons. The spatial resolution of the SEM depends on the size of the electron spots, which in turn depends on both the wavelength and the electronic-optical system. SEM was used to study the morphology of the nanostructures of the metal oxide. Scanning electron micrographs (SEM) were taken on Hitachi X650 SEM equipped with Energy Dispersive Spectroscopy (EDS).
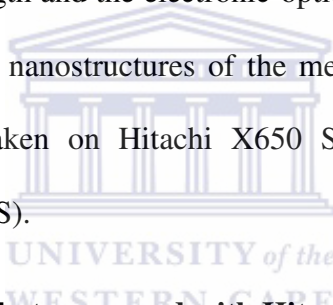
Table 3.3: The parameters that were used with Hitachi X650 SEM

SEM Parameters	Settings
Working distance	15mm
Accelerating gun ligament	Tungsten
Accelerating Voltage	25kV
Filament Current	75-80 µA

3.3.3 Electron Dispersive Spectroscopy

The elemental compositions of the catalysts were investigated using electron dispersive spectroscopy (EDS) which was connected to Hitachi X650 SEM. Each sample was scanned for 1 hour to obtain the average w.t% of the material.

3.3.4 Transmission Electron Microscopy

Transmission electron microscopy (TEM) operates on the same basic principles as the light microscope but uses electrons instead of light. TEM use electrons as "light source" and their much lower wavelength makes it possible to obtain a much higher resolution of up to 10^{-9}m.

TEM is extensively used in the investigation of particle size, particle shape and particle distribution. TEM was used to observe the morphology of the nano-structured MnO_2. Transmission Electron Micrographs (TEM) patterns were characterized by a Tecnai F20 at an acceleration voltage of 200kV.
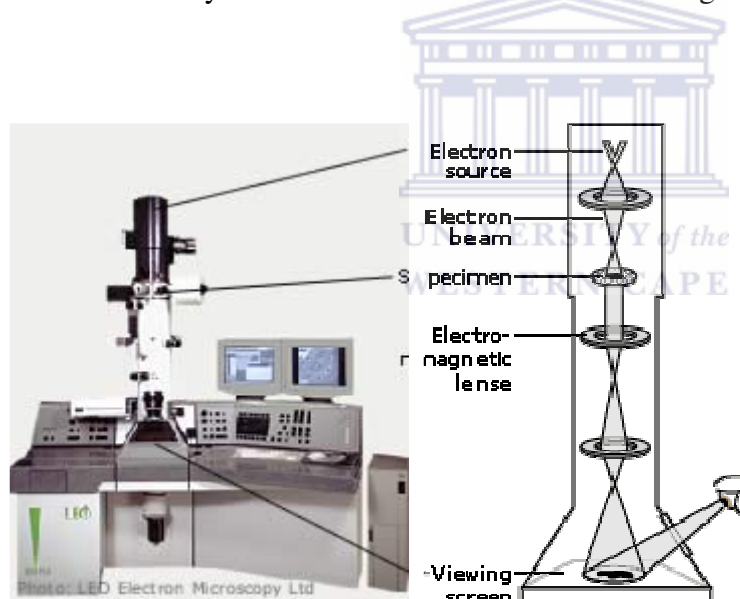
Figure 3.1: *Schematic diagram which shows direction of the electrons travelling [15].*

TEM sample were prepared by dissolving the spatula tip of the metal oxide in 5ml of methanol in glass tube, followed by sonification of the mixture for 15minutes. One drop of the mixture was deposited on the copper grid which was placed on the filtering paper. The methanol was evaporated by putting the paper under the light bulb. The samples were loaded in a sample holder.

Table 3.4: Parameters used for TEM using the Tecnai F20

TEM Parameters	Settings
Accelerating Voltage	200kV
Current	20mA
Condenser aperture	1
Objective aperture	3
Exposure time	3sec

3.3.5 Surface area and porosity determination by N_2 Physisorption

The BET theory aims to explain the physical adsorption of gas molecules on a solid surface and serves as the basis for an important analysis technique for the measurement of the specific surface area of the specific material. The amount of gas adsorbed at a given pressure allows determining the surface area. The physisorption of the molecule is determined by the following factors temperature, gas pressure, interaction between surface and gas. The monolayer adsorption is determined by the Langmuir isotherm. The multilayer adsorption is determined by the BET theory 3.2.

$$\frac{p}{v(p-po)} = \frac{1}{v_m c} + \frac{c-1}{v_m c}\frac{p}{p_o}$$

(3.2)

P and P_0 are equilibrium and saturation pressure of adsorbates at the temperature of the adsorption, v is the adsorbed gas quantity and v_m is the monolayer adsorbed gas quantity. C is the BET constant which is expressed by equation 3.3.

$$C = \exp\left(\frac{E - E_l}{RT}\right) \tag{3.3}$$

E is the heat of adsorption of the first layer; E_l is for the second and higher layers and is equal to the heat of liquefaction. Equation 1 is an isotherm and it can be plotted in a straight line as represented in figure 3.2 (1). The plot is called BET plot. The BET method is widely used in surface science for the calculation of the surface area of solids by physical adsorption of gas molecules. A total surface area S_{total} and specific surface area S_{BET} are evaluated by the following equations:

$$S_{total} = \frac{(Ns.\, v_m)}{V}$$

$$S_{BET} = \frac{S_{total}}{a}$$

Where N is Avogadro's number, s is adsorption cross section; V is the molar volume of the adsorbent gas and a is the molar mass of the adsorbed species.
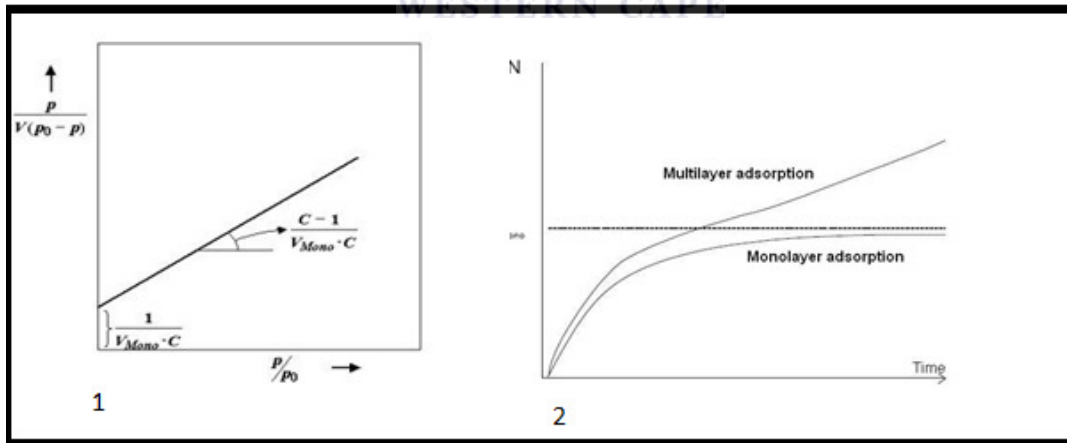

Figure 3.2: BET plot of the isotherm (1) and the plot of Langmuir and BET theories.

Nitrogen adsorption and desorption experiments were carried out at Micromeritics Tristar 3000 at 77.3 K/-195°C. The surface area was calculated using Brunauer-Emmett- Teller (BET).

Optimised samples with reaction time of 1hr, 3hr and 6 hour were tested for this analysis. About 0.2g of each sample was degassed for 30 minutes at temperature of 150^oC with nitrogen gas to remove the oxide, using the micromeritics flow prep 060. The 3 tubes containing the samples were fitted with the isothermal jacket to provide uniform nitrogen adsorption/ desorption in a temperature range of -190^oC. The test took place in Micromeritics tristar 3000 using liquid nitrogen, with atmospheric pressure at zero.

3.4 Electrochemical Measurements.

Electrochemistry is a powerful and sensitive tool used for both qualitative and quantitative analysis of the MnO_2 electrode. The most important potential application for MnO_2 electrodes is as electrochemical capacitor for energy storage/conversion. Autolab PGstat20 Echo chemie was used for electrochemical characterization. The performance and stability of the MnO_2 was studied by using fixed voltage (range between 0.1-1V) and measuring the response of the electrode. All the electrolyte solutions were bubbled under the nitrogen gas to remove the impurities and oxides before the electrochemical tests were conducted.

3.4.1 Making of the working electrode (Anode)

➢ 80% Active material (0.4g prepared MnO_2),

➢ 10% carbon black (0.05g conductor)

➢ 10% PVDF (0.05g binder).

0.05g of PVDF was dissolved in NMP via grinding in a mortar. 0.4g of MnO_2 and 0.05g of carbon black were then added slowly and ground slowly with more NMP addition. For about 30 minutes more NMP was added to form slurry, and then it was

grinded for further 30 minutes. In the mean time the piece of carbon paper current collector was put on small white tile and it was heated on the mantle at 70°C for 15 minutes. The above-prepared slurry was then pasted on the hot carbon paper using a small paint brush, it was left to dry on the mantle for further 15 minutes, the second layer of the slurry was pasted on the paper. The coated paper was dried at 100°C in vacuum oven to remove the solvent.

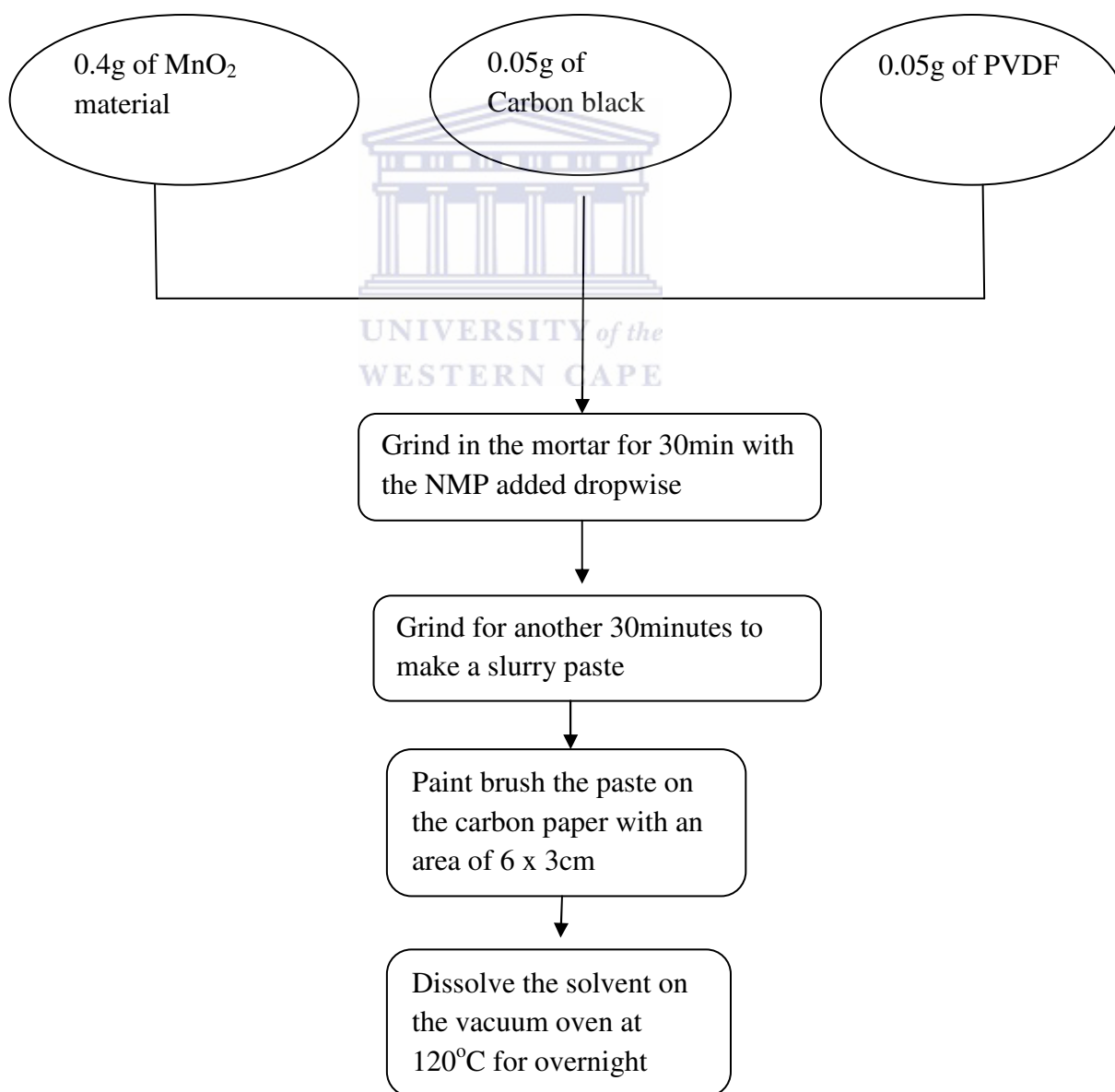A schematic electrode preparation is represented below:

Figure 3.3: *Process scheme for electrode preparation*

3.4.2 Cyclic Voltammetry

Cyclic voltammetry (CV) is the simplest form of voltammetry and consists of placing a small potential across a system and measuring the amount of current that is required, or liberated in the course of doing so. The classical form of CV was adopted which consists of the working electrode with a diameter of 12mm, a counter electrode of platinum wire with a surface area to the hundred times more than the working electrode. The third electrode in a normal three electrode system is a reference electrode, and Ag/AgCl was adopted. The system was utilised to test the electrical stability and a reactivity of molecules reacting in the electrolyte. The CV experiments were carried out in 1M Na_2SO_4 and 1M KOH to compare the results. A scan rate of 5mV/s in the range of -0.2-1.0 V was applied in every measurement at room temperature for 30 cycles. The area of the working electrode was $1.131cm^2$.

Table 3.5: The parameters that were used for CV using PGstat 20 autolab.

Working electrode	MnO_2
Reference Electrode	Ag/AgCl
Counter electrode	Pt wire
Electrolyte	1M Na_2SO_4
Scan Rate	5mV/s
Number of scans	30
Scan range	-0.2 – 1.0V

Specific capacitance (C) in F/g is calculated as anodic charge divided by voltage and normalised gram of active material

$$C = \frac{1}{m\Delta V} \int_y^x i\, dt \tag{3.4}$$

Where i is the anodic current, t is the time, x is the time when V = -0.2V and y is the time when V= 1V, ΔV is the voltage range and m is mass of the active material.

Energy storage devices, in which supercapacitors are subclass, are generally evaluated in terms of power and energy. Energy (Wh kg^{-1}) is defined as the capacity to do work, power (kW kg^{-1}) is the speed in which energy can be drawn out of, or put into a device. Equations 2.9 and 2.10 are used to evaluate the energy and the power respectively

The pseudo-capacitance in MnO_2 can be explained by two reaction mechanisms proposed for the charge storage in MnO_2-based electrodes. The first one is based on the concept of intercalation of H^+ or alkali metal cation (C^+) such as Na^+ in the electrode during reduction and de-intercalation upon oxidation [69].

$$MnO_2 + C^+ + e^- \leftrightarrow MnOOC^+ \tag{3.5}$$

The second one involves adsorption of cations in the electrolyte on the MnO_2 electrode surface [65].

$$(MnO_2)_{surface} + C^+ + e^- \leftrightarrow (MnOOC^+)_{surface} \tag{3.6}$$

At slower scan rate, Na^+ or H^+ from the electrolyte can be inserted into almost all available pores not only on the surface but also inside space of MnO_2, which lead to a high effective utilization of MnO_2 for the redox reaction and a high specific capacitance. When the scan rate is increased, the effective interaction between the ions and the electrode is greatly reduced. The effective utilization for the redox

reaction has been limited only to the outer surface of the MnO_2 electrode leading to a reduction in specific capacitance.

3.4.3 Galavanostatic charge/discharge test

The simplest capacitor that can be created is the parallel plate capacitor. A parallel plate capacitor is created by taking two conductive and applying a voltage difference between them through the use of the external circuit. Separator is used a spacer to stop the opposing electrodes from touching one another and causing a short circuit. In order to function the separator must be ionically conductive, while also electronically insulating.

3.4.3.1 Creating a SC standard test cell

Since long cycle life is very important to the SCs, the cycle charge/discharge test was employed to examine the service life of MnO_2 electrode at a current density of 200mA/g for 100 cycles. Two electrode discs with the diameter of 10mm each consisting of MnO_2 composites were assembled in a double layer cell as a cathode and an anode in the symmetric cell. The porous membrane was used as an electrolyser/separator. The separator was employed to stop the opposing electrodes from touching one another and hence causes a short circuit. The loading of the active material was calculated by difference between 10mm anode mass (prepared in 3.4.1) and 10mm of carbon cloth disc without the anode.

The cell was assembled in a small electrochemical button cell which consists of a stainless steel and copper discs (current collectors) with the same diameter as the working electrodes, but 10times more than the electrode in thickness. The two

electrodes and the separator were soaked in the electrolyte solution first before being assembles in the electrochemical cell button. The copper side was negatively charged whereas the stainless steel side was positively charged to give a galvanostatic charge/discharge curves using 1MKOH and 1M Na_2SO_4.

Table 3.6: The parameters used for charge/discharge test

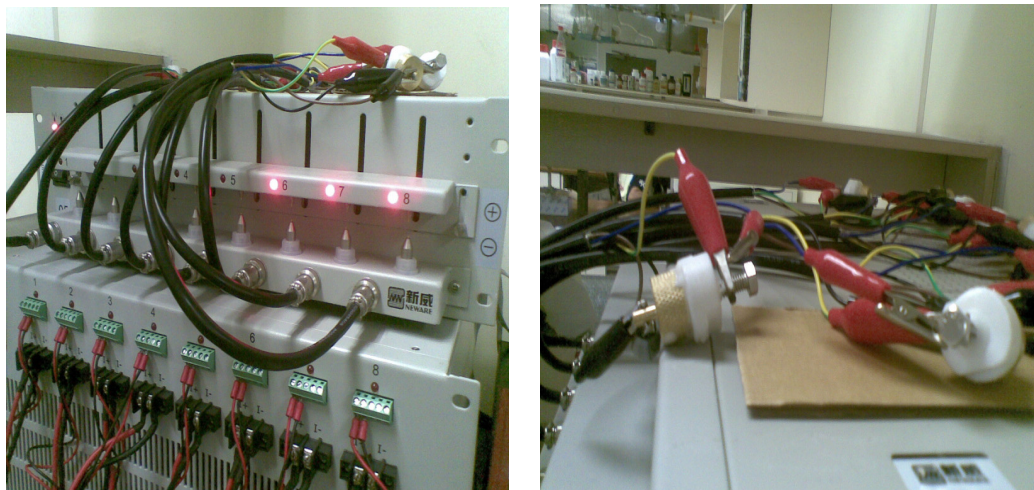| Electrolytes	1.0M Na_2SO_4 and 1.0M of KOH
Current density	200mA/g
Potential voltage window	0.1-1.0V
Separator	Gore11367985-3 (polytetrafluoroethylene)
Current Collector (+ve)	Stainless steel
Current collector (-ve)	Copper disc

Figure 3.4: *The battery testing unit equipment connected to the monitor, SCs testing button cells with red as a cathode and black as anode.*

3.5 Overview of main points
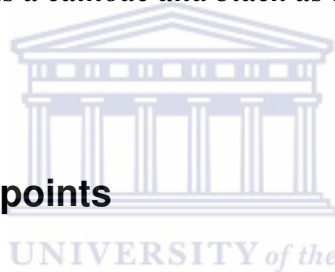
The Characterization of the electrode materials was initiated by the investigation of the structural properties using quantitative and qualitative techniques such as, SEM, TEM, EDS and XRD. Structural and electrochemical characterization and the techniques used for their study can be summarised as follows

- The elemental composition of the MnO_2 material was quantitatively studied by the EDS

- The morphological properties and degree of agglomerations of the nanostructure were studied qualitatively by SEM.

- The crystallinity and the particle size of the electrode materials were qualitatively and quantitatively studied by XRD.

- Particle shape and distribution of the morphologies of the nanostructured MnO_2 were qualitatively studied by TEM

- Total surface area and porosity of the electrode material was quantitatively studied by the N_2 absorption/desorption.

- The specific capacitance of the electrode material was measured by the CV.

- The stability and efficiency of the electrode material used in SCs was tested by the galvanostatic charge-discharge test.

Methodologies for the preparation of the nanostructured MnO_2 materials were discussed in *chapter 3*. The results of the experimental tasks that were conducted in this chapter will be discussed in *chapter 4*.

UNIVERSITY *of the*

WESTERN CAPE
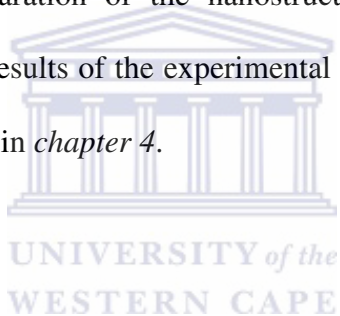
Chapter 4: Results and Discussions

In this chapter the results and interpretation of the data are discussed in detail. The investigation was initiated by structural characterization of the nanostructured MnO_2 materials synthesised under different optimal conditions. The electrochemical characterization of the electrode materials are also investigated in this chapter. The physical and electrochemical properties of the synthesised MnO_2 electrode materials are compared to those of the commercially purchased MnO_2 electrode material. The electrochemical properties are correlated with the structural studies of the electrode material.

4.1 Physico-chemical Characterization of the electrode material.

The structural characterizations were conducted as discussed in chapter 3.

4.1.1 Crystallinity and particle sizing of the metal oxide electrode

X-ray diffraction measurements were performed to examine the crystallinity of the manganese oxide electrode materials. The method for synthesising MnO_2 was optimised in order to establish the influence of the reaction time on the physical nano-structured properties of the metal oxide. To optimise the reaction time, the temperature was kept constant at 120^oC and the reaction time was varied from 1 to 6 hours. The peak structures of as-synthesised products were compared to the

commercially purchased MnO_2. Figure 4.1 shows the XRD patterns of the as-synthesised MnO_2 materials under the HT conditions.
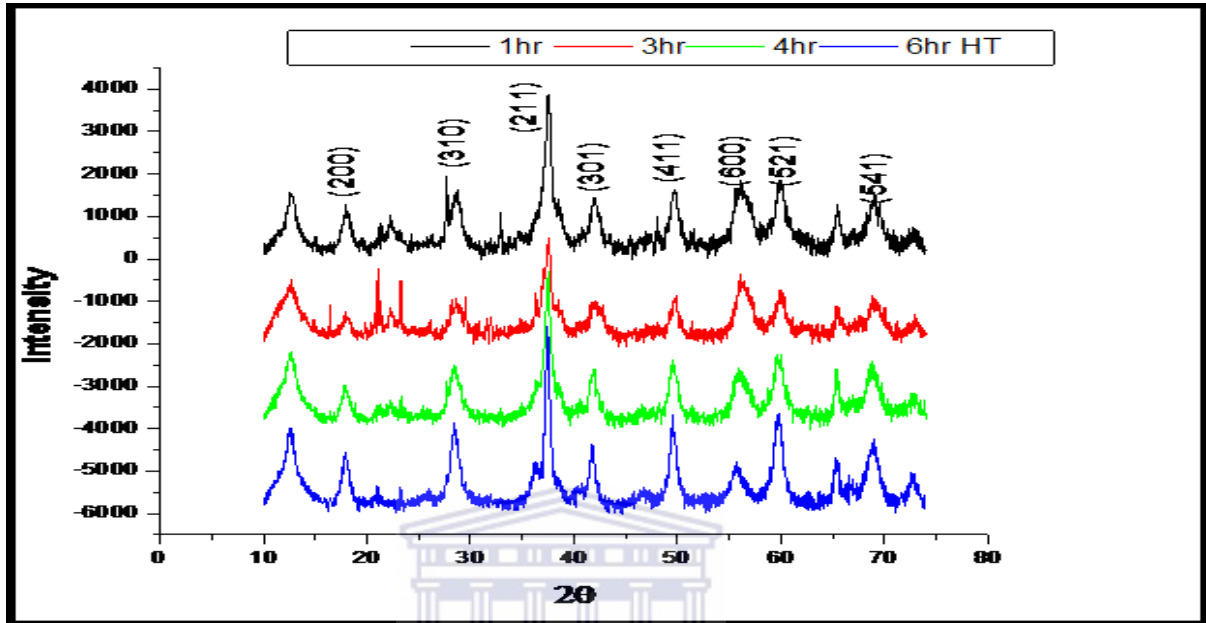

Figure 4.1: XRD patterns of optimised MnO₂ under HT conditions.

The XRD analysis reveals similar structural characteristics for the different hydrothermally reacted samples, which shows evident broad peaks at $2\theta = 37.5$ and 56.1. Other broad peaks can be observed at 12.6, 28.5, 49.8 and 68.7. These peaks are attributable to the MnO_2 phase in agreement with similar XRD patterns reported in literature. All the peaks for the samples can be indexed to a pure body-centred tetragonal α-MnO_2 phase with lattice constant a = 0.9785nm, c = 0.2863nm which are in agreement with the standard values as reported by *Chen et al* [70]. The particle sizes were determined by the Scherrer equation (3.2), it was established that the reaction time did not affect the particle size of the oxide either as the XRD patterns of both optimised MnO_2 were similar by 97%. The weak and broad peaks of this XRD patterns suggests that the tunnel structures of α-MnO_2 under hydrothermal conditions

was poorly developed, which may lead to low crystallanity. The broad and unclear peaks indicate the amorphous nature of the product.

The XRD pattern of the sample that was synthesised under LT conditions was also determined. The patterns also reveal similar characteristics for different LT time MnO_2. No characteristics peaks are observed for impurities, indicating high purity and crystallinity of the final products. Figure 4.2 shows the diffractogram of MnO_2 nanostructures that were synthesised under LT conditions.
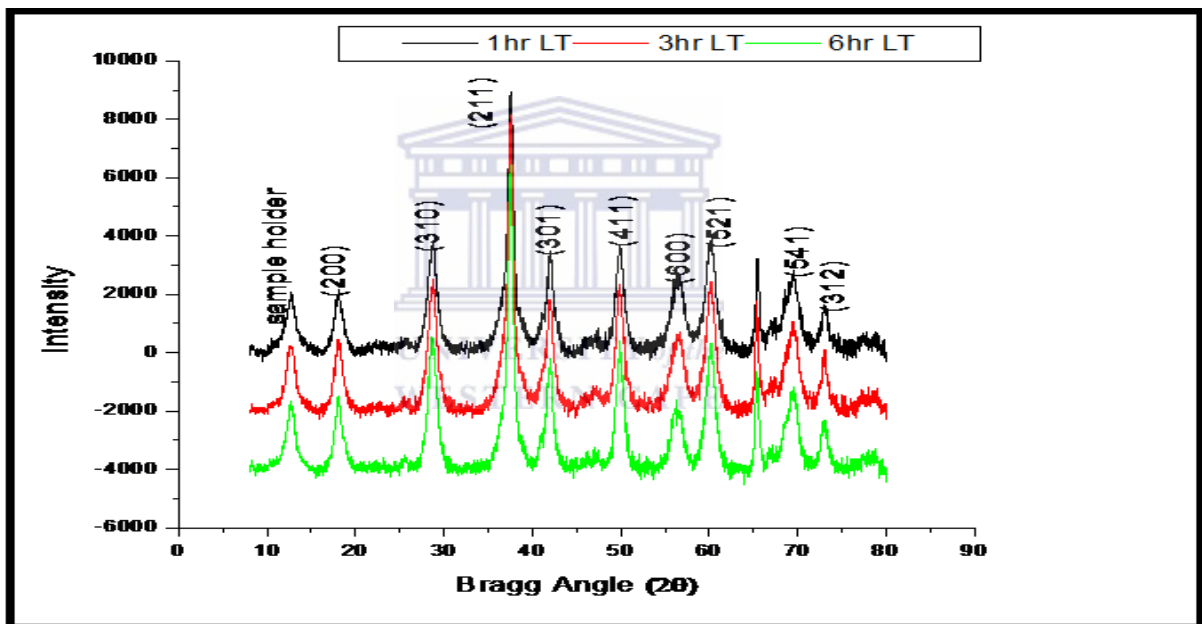
Figure 4.2: XRD patterns of MnO₂ under LT conditions.

These peaks are also attributable to the α-MnO_2 phase in agreement with similar XRD patterns reported in literature [70]. The peak recorded at 12° 2θ was credited to the x-ray beam reflecting at the sample holder, and it was observed for all sample diffractograms. The peak (211) recorded the highest intensities for both optimised samples in the diffractograms ultimately suggesting high densities of (211)-orientated crystals. The particle size was calculated by using equation 3.1, and the sizes of the particles were not time-dependant on synthesis, the particle size of optimal manganese

oxides gave 98% efficiency. The particle sizes of the MnO_2 optimised under HT conditions were found to be slightly bigger than those optimised under LT conditions.

Table 4.1: Calculated particle size of the tetragonal α-MnO_2

α-MnO_2 peak	Particle size (Å) LT	Particle size (nm) LT	Particle size (Å) HT	Particle size (nm) HT
(200)	4.63	0.463	4.67	0.467
(310)	3.15	0.315	3.20	0.320
(211)	2.11	0.211	2.15	0.215
(301)	1.89	0.189	1.91	0.191
(411)	1.59	0.159	-	-
(521)	1.32	0.132	-	-

The XRD data of the commercial MnO_2 showed the intermediate broad diffraction peaks at 2θ = 22.1, 37.2, 42.55, and 56,4 being observed. This crystalline phase can be indexed to orthorhombic γ-MnO_2 reported by *Gao et al*[18]. The intense peaks reflections suggest that the tunnel structure of orthorhombic γ-MnO_2 was properly developed. As can be seen from Figure 4.3 that the reflection of γ-MnO_2 at facets (131), (300) and (161) are sharp and intense, implying a gradual crystallization.
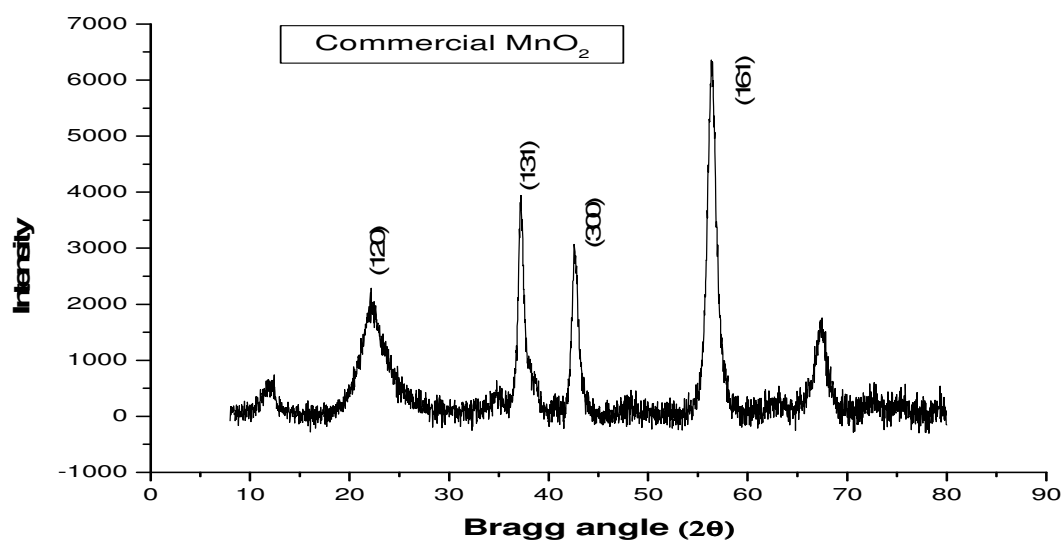
Figure 4.3: XRD pattern of the commercial MnO$_2$

4.1.2. Morphological characterizations and agglomeration states of the nano-structured metal oxide.

The nano-morphological feature aspect of the material is depicted by SEM images in Figure 4.4. In order to understand the effect of reaction time on the sample morphology, the sample shape was recorded after a suitable reaction time ranging from 1 to 6 hours. As can be seen from Fig. 4.4 (a-c) the MnO$_2$ obtained at hydrothermal reaction shows some small nanorods formed on the surface of MnO$_2$ sphere. The hydrothermal reaction time does not seem to have any effect on the morphological features of the MnO$_2$ nanorods, the morphological diameter of the nanorods is 1-2 µm. The morphology of MnO$_2$ synthesised under low temperature conditions are represented in Figure 4.4 (d-f). They yielded nanorods with the uniform diameter of 0.5-1.0 µm. The nanorods of the α-MnO$_2$ have urchin-like structures, and the SEM analysis couldn't spot any differences in terms of morphological structures of optimal electrode.

Fig 4.4a: SEM HT MnO$_2$ after 1hr
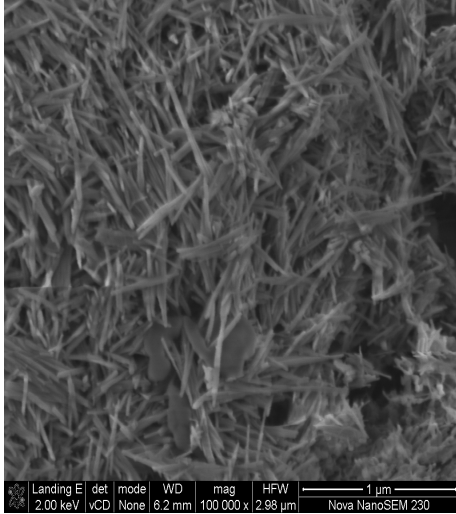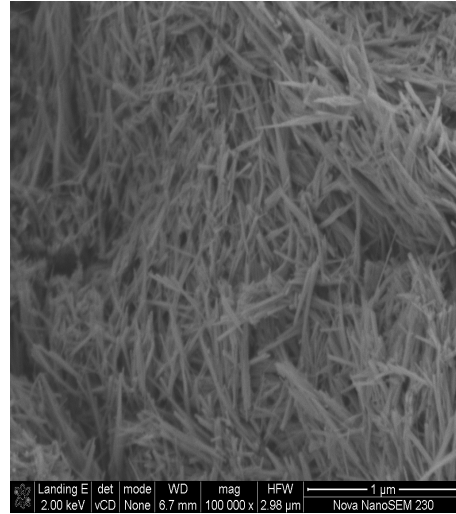

Fig 4.4b: SEM HT MnO$_2$ after 3hrs

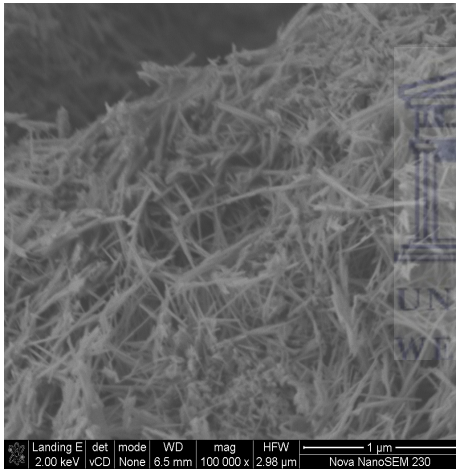*Fig 4.4c: SEM HT MnO$_2$ after 6hrs*
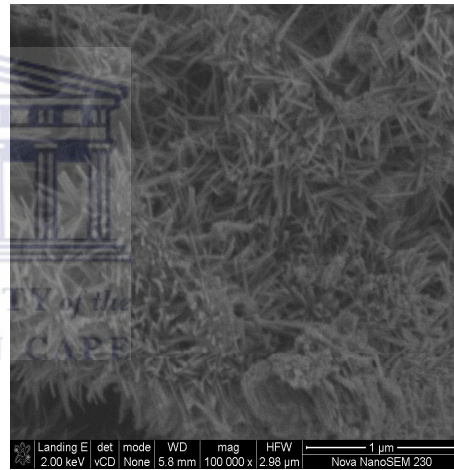
Fig 4.4d: SEM LT MnO$_2$ after 1hr
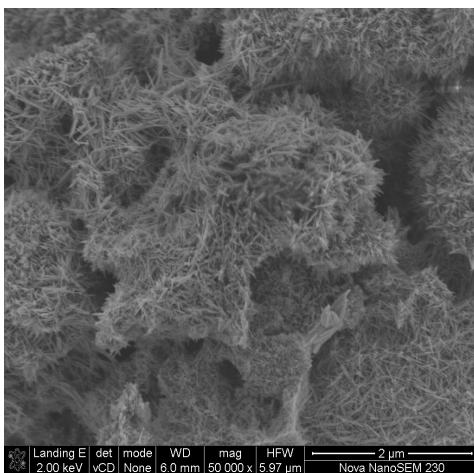
Fig 4.4e: SEM LT MnO$_2$ after 3hrs
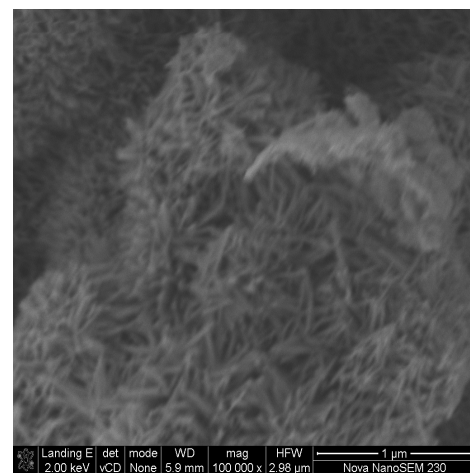
Fig 4.4f: SEM LT MnO$_2$ after 6hrs

The EDS analysis was used to study the elemental distribution of the MnO_2 materials. Figure 4.5a shows the spectroscopy of the material that was synthesised under hydrothermal conditions as indicated in chapter 3.2.2, the spectroscopy shows that the MnO_2 sample contained some few traces of the sulphur (S) element in mixing with the accepted manganese and the oxygen element. This due to the fact that the reagents that were used for co-precipitation of the electrode material consisted of the S element as specified at section 3.2.2. The spectroscopy of the electrode material that was synthesised under low temperature condition as indicated in section 3.2.1 is represented in Figure 4.5b. The spectroscopy shows traces of the potassium (K) element which was used in $KMnO_4$ as a reduction agent.
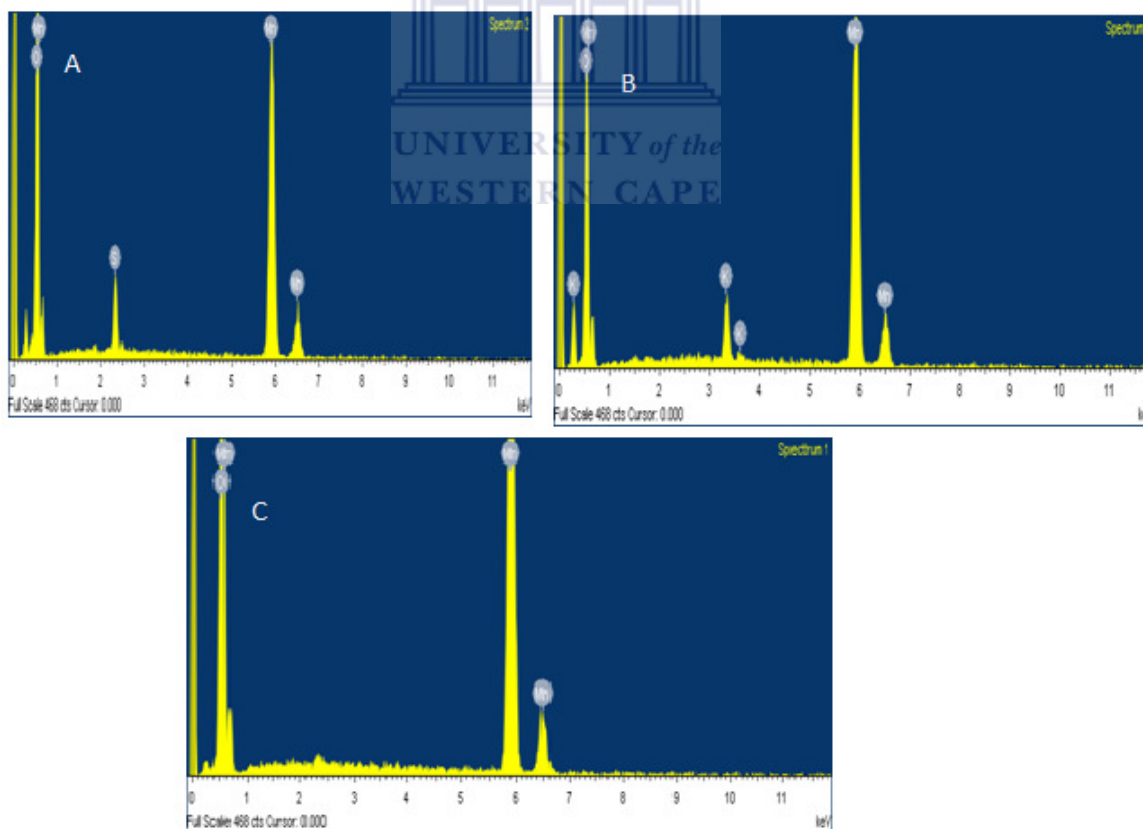
Figure 4.5: The EDS spectroscopy of (A) HT MnO_2 (B) LT MnO_2 and (C) Commercial MnO_2

The compositions of the electrode material synthesised under various conditions are presented in Table 4.2. All the elemental decomposition of the atomic structure of the MnO_2 showed the ratio of Mn and O to be 1:2, the theoretical elemental decomposition of Mn and O_2 is 63.19% and 36.81% respectively; and the results also showed the reaction time doesn't have any significant effect on the elemental decomposition of the electrode material.

Table 4.2: Elemental compositions study obtained with EDS

	LT 1hr		LT 3hr		LT 6hr	
Element	Atomic %	Weight %	Atomic %	Weight %	Atomic %	Weight %
Mn	32.65	61.50	31.43	60.01	33.81	61.54
O	65.39	35.87	66.26	36.84	57.39	28.64
K	1.96	2.63	2.32	3.15	8.80	9.82

	HT 1hr		HT 3hr		HT 6hr		Commercial	
Element	Atomic %	Weight %	Atomic %	Weight %	Atomic %	Weight %	Atomic %	Weight %
Mn	29.61	57.83	36.51	63.99	26.42	52.91	31.17	60.86
O	66.67	37.92	55.80	28.37	66.46	38.76	68.83	39.14
S	3.73	4.25	5.24	5.36	7.12	8.32		
Al			2.66	2.29				

The EDS of the commercial MnO_2 electrode material showed the material to be pure without any elementary traces found as shown in the above data (Table 4.2). The SEM images of the commercial MnO_2 are presented in Figure 4.6.
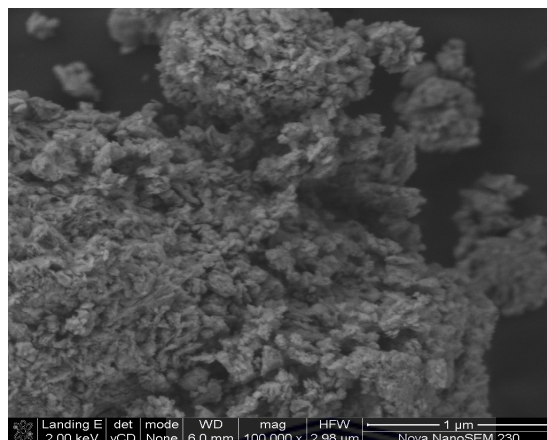
Figure 4.6: SEM image of the commercial MnO₂

The SEM image showed the spherical aggregates, growth of the particle was still in the developing stage of forming nanorods, which could mean that the material was synthesised at lower reaction temperatures or shorter reaction time, this theory is in agreement with the γ-MnO_2, which is usually the least stable of the polymorphs. The growth of the γ-MnO_2 can be promoted by either increasing the reaction temperature or prolonging the reaction time, in which the former process is dominant [18]. By changing as previously discussed parameters usually leads phase structural transformation from γ to β-MnO_2, which is more stable. The existence of the spherical aggregates suggests a homogenous nucleation process of γ-MnO_2

4.1.3 Electrode particle size and distribution

In order to understand the effect of reaction time on the sample morphology and the forming mechanisms of the different structured MnO_2, the sample obtained from different reaction time were analysed by the TEM. As can be seen from Figure 4.7 (a-

e), several evolutions stages could be clearly observed. The products obtained by low temperature reaction at 1 hour are solid nanosphere structures with interleaving nanowhiskers. After reaction for 3 hours, the nanowhiskers spheres transform to flower-like nanostructures which consists of some nanorods on the surface. When prolonging to 12 hours, the interior cavity sphere is easily observed. The rod diameter and length of MnO_2 array could be estimated to be approximately $1.0\mu m$ and $200nm$ respectively. The TEM image of the α-MnO_2 under the hydrothermal conditions is represented by Figure 4.5 (a-c).
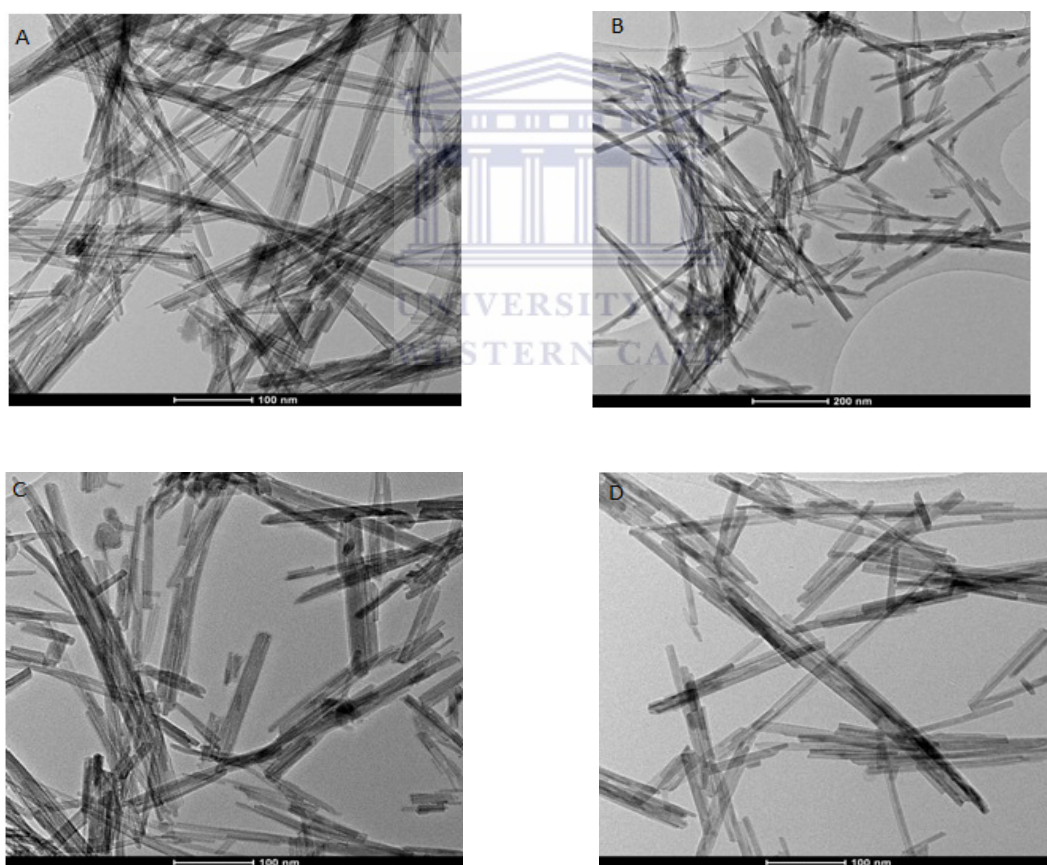
Figure 4.7: TEM images of as-prepared MnO_2 at different low temperature dwell times: (A) 1hr, (B) 3hr, (C) 5hrs and (D) 6hrs

In terms of the below evolution of time dependent morphology, an "Oswald ripening process" could be used to explain the formation of the different structured α-MnO_2

[71-73]. During the hydrothermal reaction procedure, a large number of nuclei are formed in a short time, and a slow crystal aggregate follows to form a sphere with a solid core. This stage might last for several hours till an interior cavity is gradually formed via a core evacuation process due to higher surface energy [18]. A subsequent increase in the hydrothermal dwell time leads to a subsequent dissolution-recrystallization process in which the amorphous components in the agglomerates would dissolve again and grow into nanorods. The larger nanorods grow at the cost of the ones in thermodynamically stable environment and urchin structures are damaged completely into many individual nanorods.
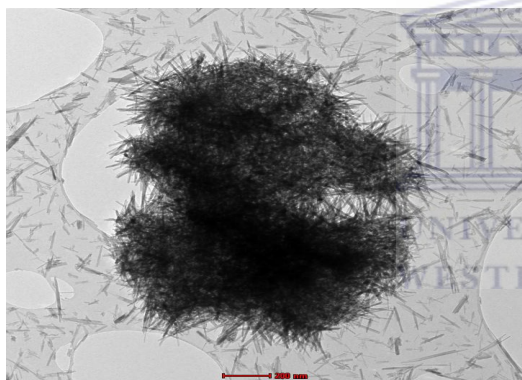

Figure 4.8a: TEM of 1hr HT MnO₂
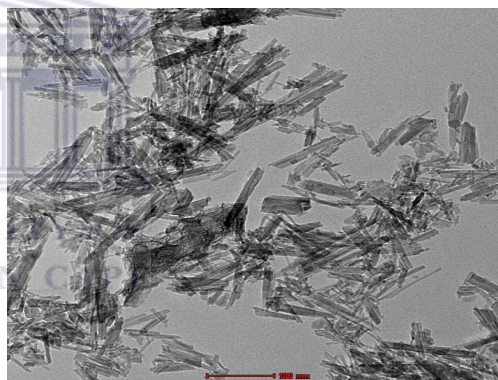
Figure 4.8b: TEM of 3hr HT MnO₂
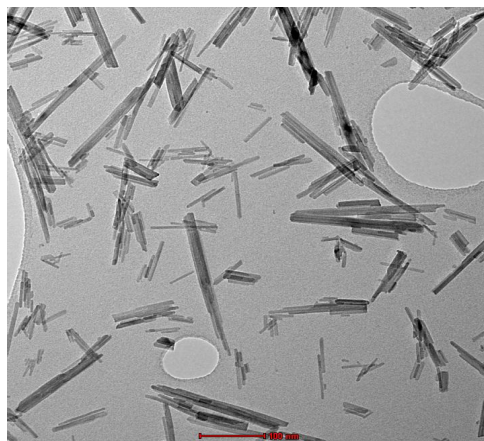
Figure 4.8: TEM images of α-MnO₂ at different HT dwell time (a) 1hr, (b) 3hr and (c) 6hr

The TEM image of the commercial material is represented in Figure 4.9. The MnO_2 is very loose and being consisted of many small particles, confirming that this material is consisted of significant amount of amorphous materials with a little nano-crystalline grain.
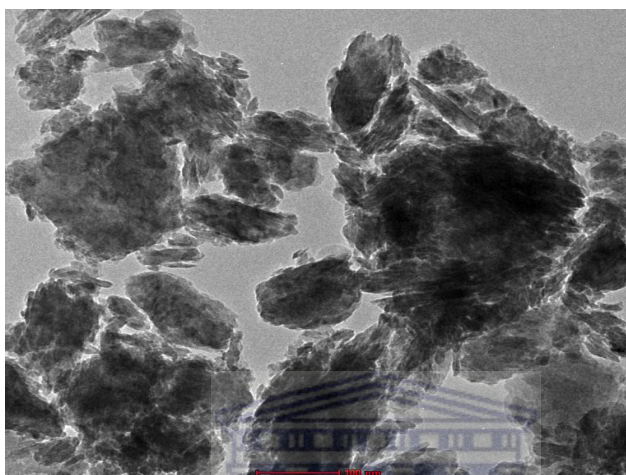
Figure 4.9: TEM image of the commercial γ-MnO₂ nano-structural material.

4.1.3. Determination of the surface area of the nano-structured metal oxide

N_2 adsorption-desorption studies were performed to determine the specific surface area of the MnO_2 prepared at different optimal times. The BET surface areas of as-synthesised α-MnO_2 are represented in Table 4.3. Figure 4.10 and 4.11 shows the nitrogen adsorption-desorption isotherms of the α-MnO_2 under the HT and LT conditions respectively. The pore size distributions calculated from the isotherms are also represented in Table 4.3. The specific surface area is more dependent on the pore structures which in return are dependent on the morphologies and nanostructures of prepared MnO_2. As it was explained earlier under the TEM analysis in the forming mechanism of α-MnO_2, the materials prepared under low temperature from 1 to 6hours as represented by Figure 4.7 (a-c) has almost similar structures, which shows

that the optimal conditions had less effect on the morphology of the α-MnO_2 for that period, hence the BET surface area recorded for those specific materials showed almost the same values of 130.38, 129.2 and 127.08 m^2/g respectively.

For the materials prepared under hydrothermal conditions, as explained previously, the materials prepared for 1 hour exhibit more agglomerated solid structures, while when prolonging the reaction time to 3 hours, the solid structures becomes loose urchin-like structure, leading to a decrease in specific surface area. After reaction of 6 hours, the specific surface increases to 60.17 m^2/g because of urchin-like structures transformed to densely aligned nanorods. The surface area is also dependent on the pore length, the shorter pore length the higher the specific surface area as it was shown in equation 3.7. The special high BET surface area and porous structure of the urchin-like α-MnO_2 provide the possibility of efficient transport of electrons and ions, which cause high electrochemical capacity of these materials.

Table 4.3: Total BET specific surface area of the MnO_2 and the pore diameter.

Sample (Low Temperature)	Surface Area (m^2/g)	Pore diameter (nm)	Sample (Hydrothermal)	Surface Area (m^2/g)	Pore diameter (nm)
MnO_2 1hr	130.38	0.9487	MnO_2 1hr	54.97	11.22
MnO_2 3hr	129.2	0.9766	MnO_2 3hr	33.45	15.97
MnO_2 6hr	127.08	0.9292	MnO_2 6hr	60.17	14.66

The Langmuir isotherm adsorption/desorption plots of products are represented in Figure 4.7 and 4.8.
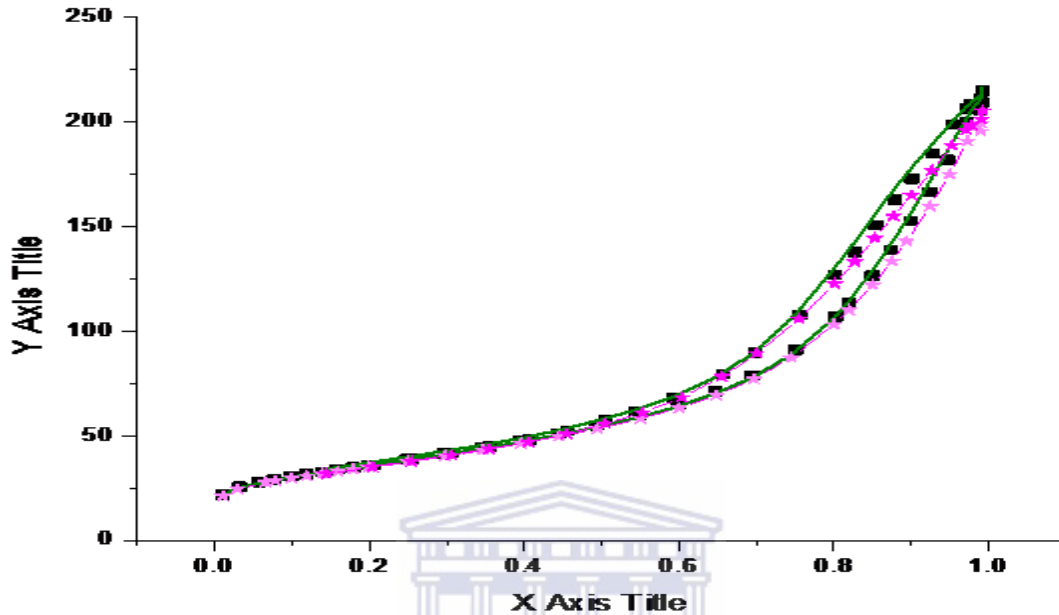

Figure 4.10: *Langmuir isotherm plot LT conditions, olive green solid line= 3hr LT MnO2, black scattered = 1hr LT MnO2 and pink line with symbols = 6hr LT*
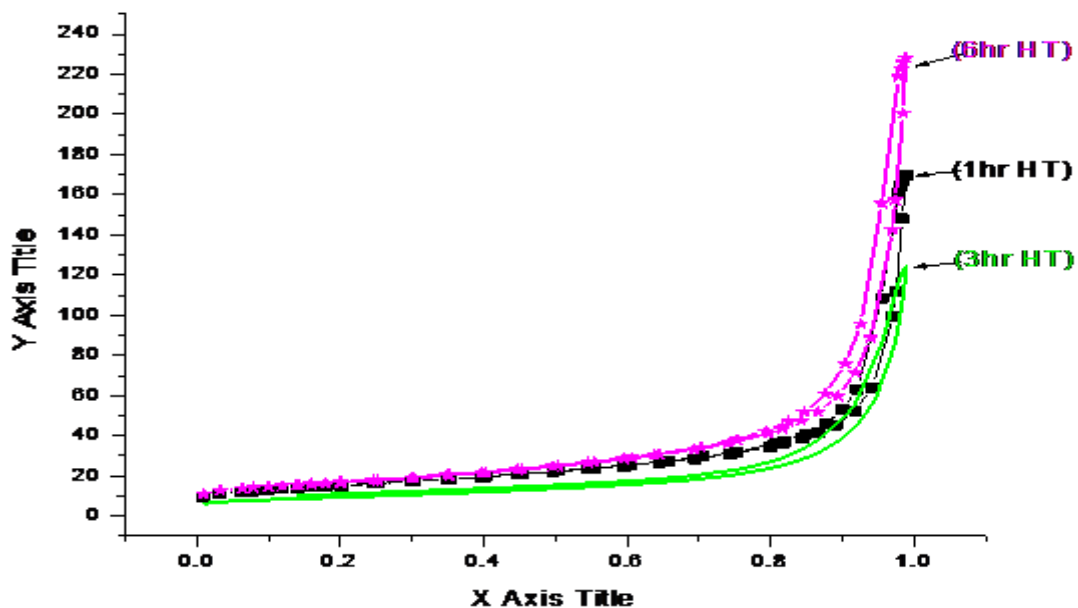
Fig 4.11: *N_2 Adsorption-desorption Langmuir isotherm hydrothermal conditions; Black scattered line = 1hr, Green solid line = 3hr and Pink star = 6hr HT*

4.2. Electrochemical characterization

The most important application of MnO_2 nanostructures is as electrochemical capacitor for energy storage/ conversion. The capacitance of MnO_2 capacitor primarily arises from redox transition of MnO_2 active material; it is due to a Faradic charge transfer reaction at the interface of the electrolyte and the electrode. Electrochemical properties of the synthesised MnO_2 nanostructures were characterised by cyclic voltammetry and charge-discharge test. The electrochemical characterizations of the synthesised MnO_2 will be compared with the purchased MnO_2. The electrode was prepared as discussed in section 3.4, and the parameters used for the measurements are also discussed in that particular section.

4.2.1 Determination of the pseudo-capacitance of the MnO_2

Cyclic voltammograms recorded at a scan rate of 50mV/s in the 1M Na_2SO_4 electrolyte for MnO_2 for different times are shown in Figure 4.12 (a) and (b). The figures show that both different methods produced different voltamograms with different shapes. The curves shows there was no visible redox reaction peaks in the - 0.2 – 1.0 potential rate. The specific capacitance can be evaluated from the area under the CV curve. The cycle efficiency of the capacitance was very impressive after the 30th cycle. The calculated values of the specific capacitance are represented in Tables 4.5 and 4.6. The specific capacitance was calculated using equation 3.4 in section 3.4.2. The area of the working electrode was 1.131cm^2.

Table 4.4: calculated specific capacitance values of hydrothermal

Sample duration (hrs)	Loading (g)	Area density (mg/cm^2)	Specific capacitance (F/g)
1	0.00144	1.273	41.56
3	0.00104	0.920	38.36
6	0.00136	1.202	58.67

As observed from Table 4.4 that the manganese electrodes synthesised under hydrothermal conditions yielded a lower specific capacitance, with the 3 hour optimal sample yielding the lowest. This could also due to the fact that they both had different physical characterization structures. The BET surface area of the sample prepared under after 3 hour was the lowest and it yielded the nanostructures with longer diameters. There diameters were lower than those prepared under low temperature conditions, as discussed earlier in chapter 2 that the larger surface area indicates higher accessibility of the active material, leading to a better capacitive behaviour. Optimal sample 3 of hydrothermal conditions in Table 4.5 yielded the lowest capacitance value as the surface area of the particular sample was the lowest.

Similar results have been observed in the case of the time-dependent and temperature-dependent capacitance for MnO_2 prepared at different conditions [17, 21, 22]. The main difference in the specific capacitance may be attributed to the different crystallinity, morphologies, nanostructures, specific surface area, co-existence of more metal ions such as K^+, and the loss of the chemically and physically adsorbed water from MnO_2 [1, 13, 14, 17, 23, 24].

Since the method of coating the electrode to the carbon paper was paint brush, it was hard to achieve the similar range of coating and as discussed earlier (section 2.5.1.3) that the loading also has an effect on the specific capacitance rate. The higher loading, yield the low specific capacitance, which could explain why Table 4.6 has varying specific capacitance values yet the physical structures of the optimal samples were more or less similar.

Table 4.5: Calculated Specific capacitance values of low temperature

Sample duration (hrs)	Loading (g)	Area density (mg/cm^2)	Specific Capacitance (F/g)
1	0.00184	1.627	95.4
3	0.00164	1.450	121.64
6	0.00140	1.238	178.6

The annealing temperature of the hydrothermally prepared MnO$_2$ was 120°C as the resultant precipitant was too wet and it required a higher and longer drying time. The loss of water content during the annealing resulted in shrinking of the product, which resulted in decrease in the surface area and hence it vitally hinders the electrochemical activity as reported by Zhang et al [19]. Consequently loss of water contents leads to the loss of pseudocapacitance. Figure 4.12a and b represents the voltamograms of LT MnO$_2$ and HT MnO$_2$ respectively. The curves show no clear peaks which means the electrodes were charged and discharged at a pseudoconstant rate over the voltammetric cycle. At low scan rate (Figure 4.13) of 5mV shows almost the ideal capacitive behaviour.
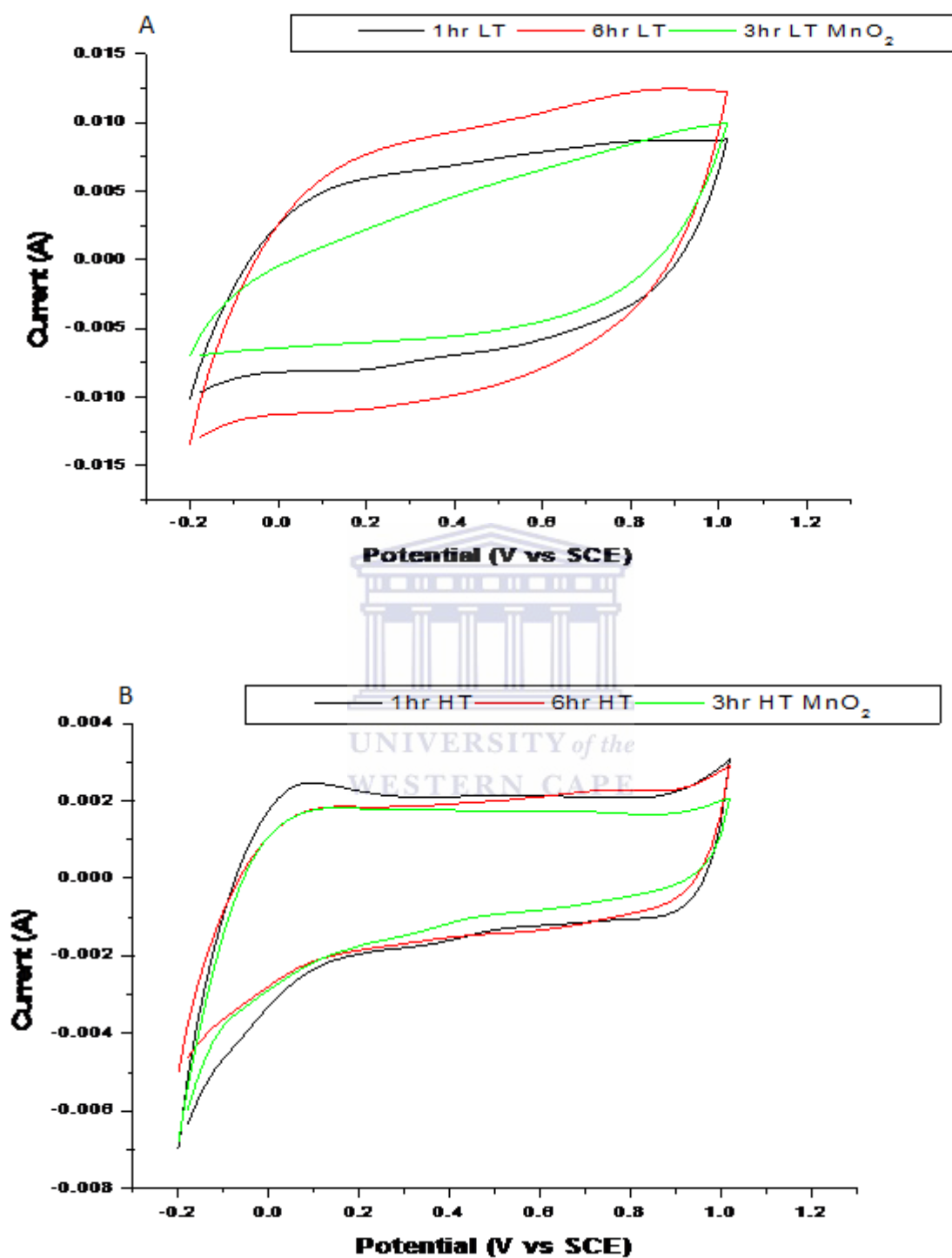
Figure 4.12: *(A) Cyclic voltamograms of MnO₂ nanostructures at different dwell times synthesised under low temperature conditions, (B) under hydrothermal conditions (with 1M Na₂SO₄ at room temperature at 50mV/s)*
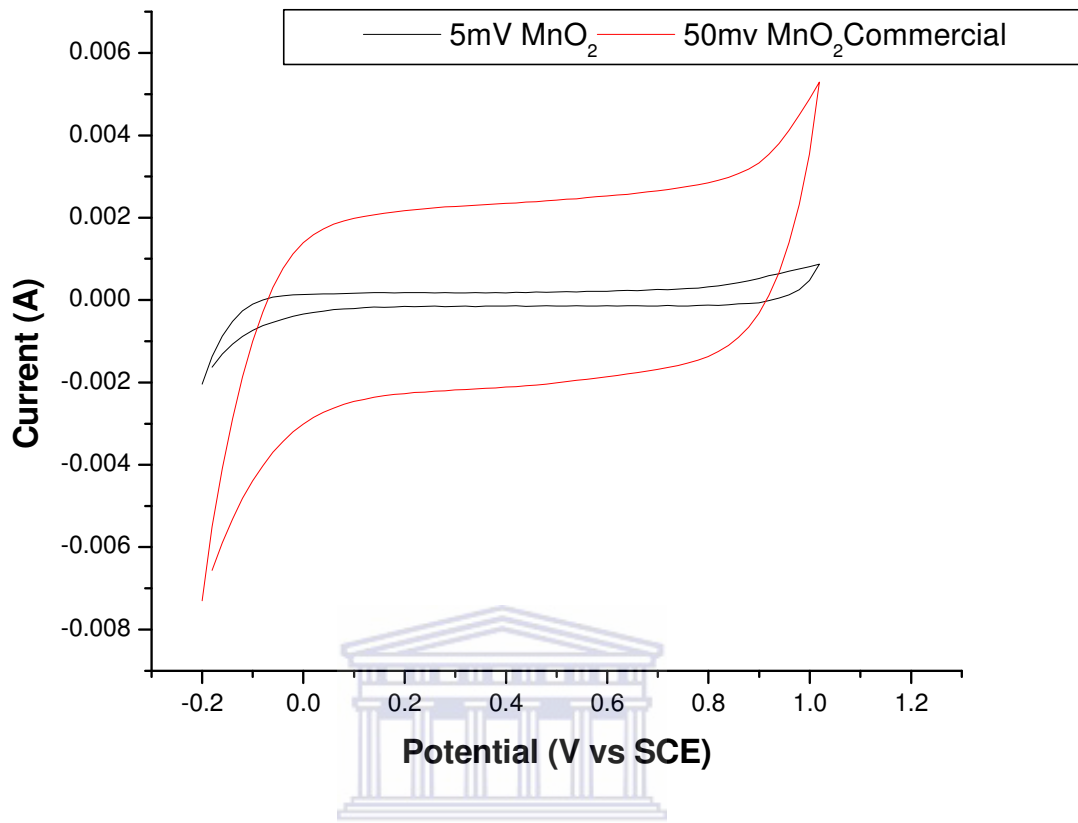
Figure 4.13*: The voltamograms of the commercial MnO$_2$ at different scan rates (with 1M Na$_2$SO$_4$ at room temperature).*

The effect of the scan rate was studied at different scan rates in the 1M Na$_2$SO$_4$ electrolyte for the commercial sample. The specific capacitance at scan rate of 5mV is 88.1F/g and at scan rate of 50mV gave 53.48F/g. At low scan rate (5mV/s), the MnO$_2$ shows almost an ideal capacitive behaviour. With the scan rate increasing, the deviation from rectangularity of the CV becomes obvious. Figure 4.13 represents the cyclic voltammograms of the commercial MnO$_2$. The following common features are observed. These curves show no peaks.

4.2.2. Assembling and testing the supercapacitor with MnO$_2$ composites

The charge-discharge test is one of the most reliable experiments to evaluate the specific capacitance. To test for the long term stability of the component charge-discharge test is always a useful tool.

4.2.2.1 Charge-discharge test of the prepared MnO$_2$ under hydrothermal conditions

Figure 4.14 (a-b) shows the cycle life curve and the specific capacitance plotted curve of the α-MnO$_2$, the cell was assembled as discussed in section 3.4.3.1. The long term stability of the composite electrode made of material obtained at 1 hour, and the variation of specific capacitance of 100 cycles is depicted in Figure 4.9. The first cycle charge and discharge capacities obtained were 20.89 mAh/g and 13.61 mAh/g respectively, giving cycle efficiency of 65.2%. The second cycle gives capacitance of 18.78mAh/g and 12.95mAh/g with cycle efficiency of 68.9%. The 100th cycle reversible charge and discharge capacities obtained for 1 hour HT MnO$_2$ were 14.56 mAh/g and 11.7 mAh/g respectively, giving 80% cycle efficiency for the 100th cycle. The capacitance values are listed in Table 4.6 for the 1st, 2nd and 100th cycle and were calculated using equation 1.

$$C = \frac{3.6\,Q}{\Delta V} \qquad\qquad (1)$$

Where C = Capacitnace in F
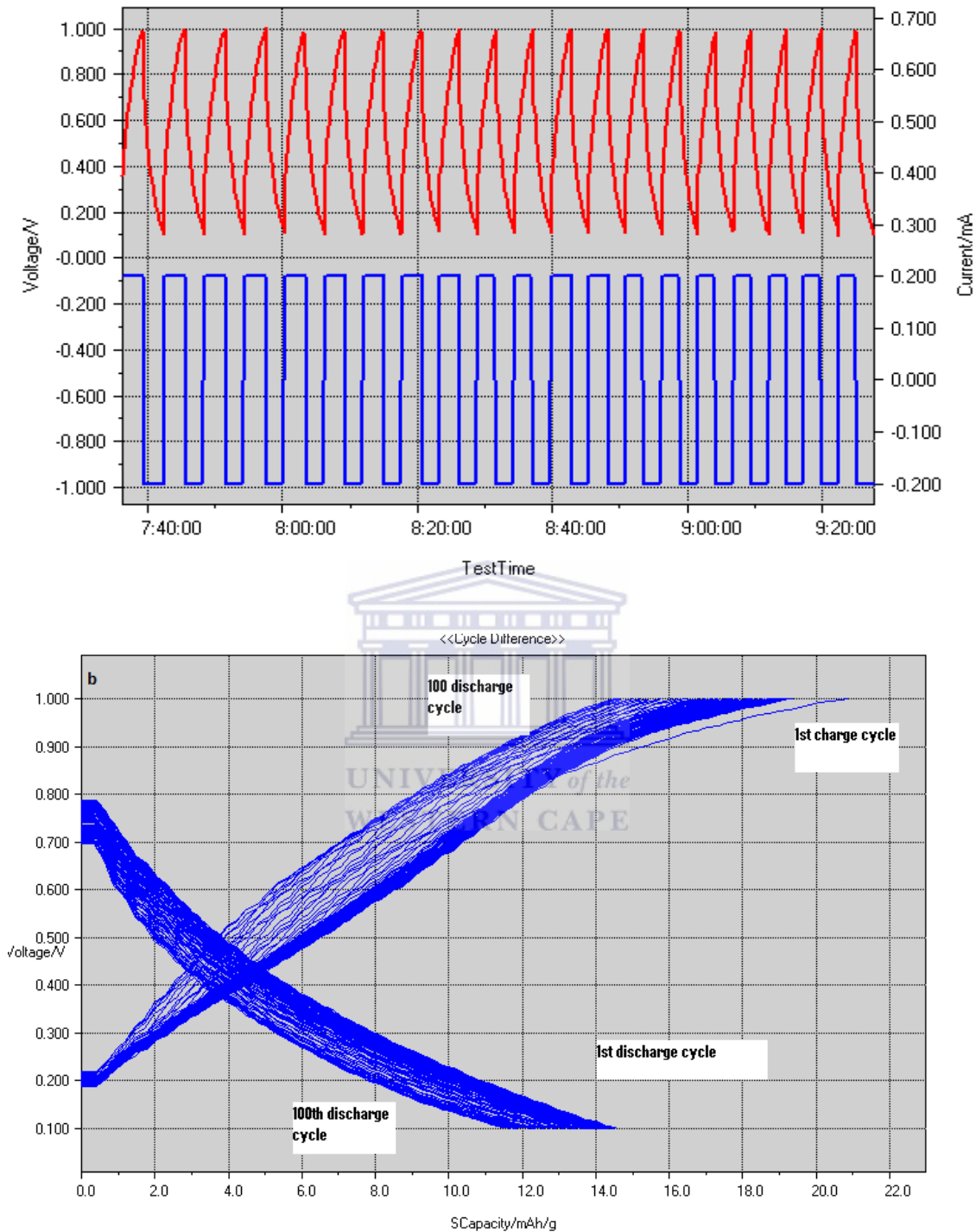
Q = Capacity in mAh/g

ΔV = Voltage difference in V

Figure 4.14: *The charge and discharge of the 1hr HT condition α-MnO₂ at constant current 200μA; (b) Cycle life of the commercial MnO₂ in 1M Na₂SO₄ between 0.1 and 1.0V.*

After 100 cycles, the capacitance is only 70% of the first cycle. This demonstrates under the voltage of 0.1-1.0V, there was not much significant decomposition which affected the microstructural changes of the α-MnO$_2$ electrodes. The long-term stability of the material implies it is a good candidate for supercapacitor application as Tang Et Al [69] reportedly obtained 87% efficiency.

Table 4.6: Capacity and Capacitance values of 1 hour HT

Cycle Number	Charge Capacity (mAh/g)	Charge Capacitance (F/g)	Discharge Capacity (mAh/g)	Discharge Capacitance (F/g)	Cycle efficiecy
1	20.89	83.56	13.61	60.8	65.2%
2	18.78	75.12	12.95	59.6	68.9%
100	14.56	58.24	11.7	46.4	80%

The capacitance cycle life of the 3 hour α-MnO$_2$ under HT conditions is represented by Figure 4.10. The specific capacitance of the first cycle of the charge and the discharge is 23.23mAh/g and 21.84mAh/g, with cycle efficiency of 94%. The second cycle yielded the charge and discharge of 22.27 and 21.13mAh/g respectively, with the cycle efficiency of 95%.

The 100th cycle reversible charge and discharge capacitance obtained was 9.36 and 9.28 mAh/g, with a cycle efficiency of 99%, after 100 cycles, the specific capacitance was only 40% of the first cycle. Which means the 3 hour HT MnO$_2$ had a very good short term stability of charging and discharging, but yielded very poor long term stability as there was 60% loss of the initial capacitance. Table 4.7, below shows the capacitance values and cycle efficiencies.

Table 4.7: Capacitance values of the 3 hour MnO$_2$ at HT conditions

Cycle Number	Charge Capacity (mAh/g)	Charge Capacitance (F/g)	Discharge Capacity (mAh/g)	Discharge Capacitance (F/g)	Cycle efficiency
1	23.23	92.92	21.84	87.36	94%
2	22.27	89.08	21.13	84.52	95%
100	9.36	37.44	9.28	37.12	99%
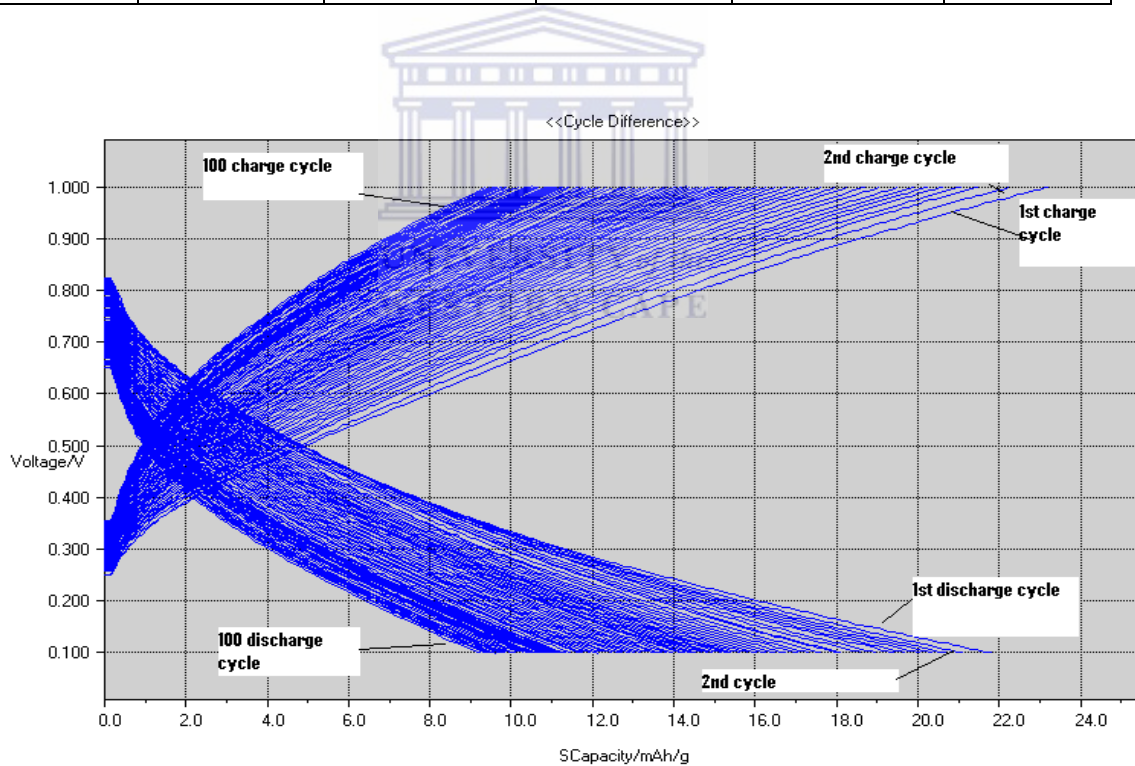
Figure 4.15: *The capacitance cycle life of the 3hr MnO$_2$ under HT conditions, with 1M Na$_2$SO$_4$*

The long term stability of the 6 hour MnO_2 under HT condition, and its variation of specific capacitance is depicted in Figure 4.16. The charge and discharge specific capacitance of the first cycle yielded 33.1 and 32.1 mAh/g respectively, with a cycle efficiency of 97%. The second cycle yielded the charge and discharge of 33.0 and 31.9 mAh/g respectively, with the cycle efficiency of 96.7%. The 100th cycle reversible charge and discharge capacitance obtained was 20.9 and 20.9 mAh/g, with a cycle efficiency of 100%, after 100 cycles. The specific capacitance of the 6 hour HT MnO_2 after 100 cycles was 63% of the first cycle. This demonstrates that within the voltage window of 0.1 and 1.0, the charge and discharge do not seem to induce significant structural changes of the α-MnO_2 electrode material as expected for the pseudocapacitance reaction. The long term stability implies that the 6hr HT α-MnO_2 is a good candidate as a material for supercapacitors. Table 4.8 indicates the capacitance values of the 6 hour MnO_2 at HT.

Table 4.8: Capacitance values of the 6hr MnO_2 at HT conditions

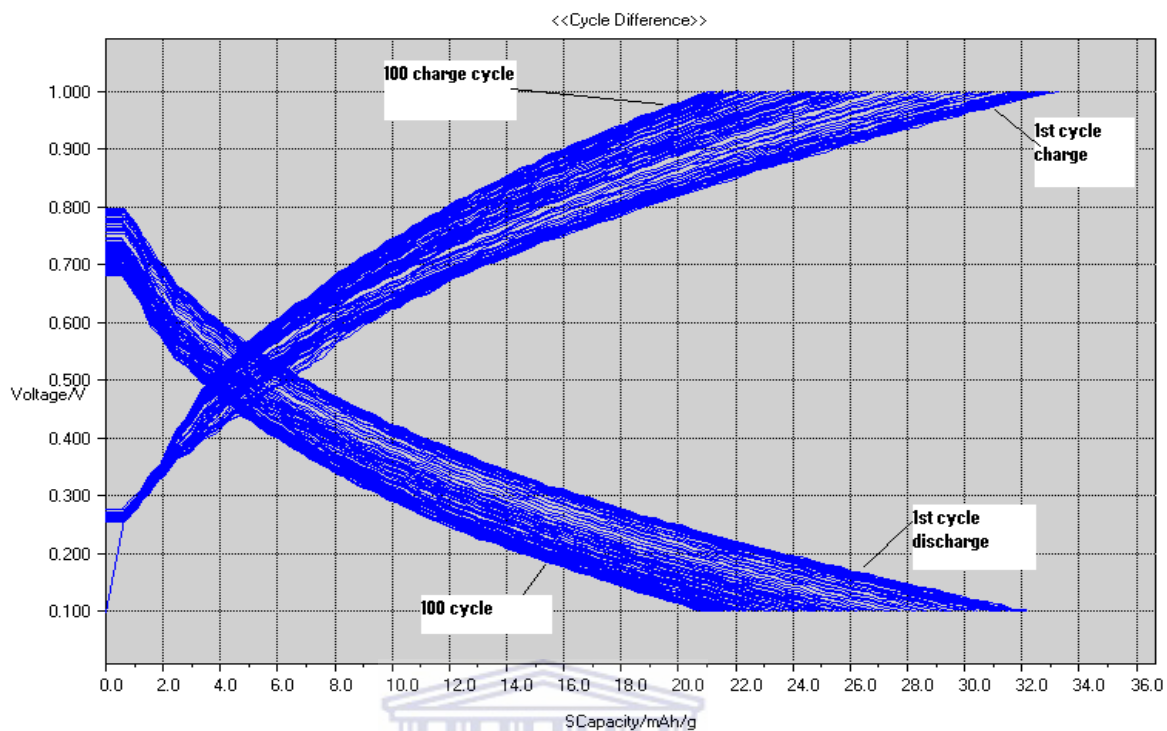| Cycle Number	Charge Capacity (mAh/g)	Charge Capacitance (F/g)	Discharge Capacity (mAh/g)	Discharge Capacitance (F/g)	Cycle efficiency
1	33.1	132.4	32.1	128.4	97%
2	33.0	132	31.9	127.6	97%
100	20.9	83.6	20.9	83.6	100%

Figure 4.16*: Specific capacitance cycle life of the 6hr HT MnO$_2$, with 1M Na$_2$SO$_4$.*

4.2.2.2. Charge-discharge test of the Low temperature (LT) prepared MnO$_2$

The charge and discharge test of the MnO$_2$ electrode material prepared under LT conditions was assembled as previously explained in section 3.4.3.1. The long term stability of the composite electrode material made of powder obtained at 1 hour, and the variation of specific capacitance of 100 cycles is depicted in Figure 4.17. The first cycle charge and discharge capacities obtained were 33.11 mAh/g and 24.10 mAh/g respectively, giving cycle efficiency of 73%. The second cycle yielded the charge and discharge of 28.13 mAh/g and 23.01 mAh/g respectively, with cycle efficiency of 81.8%. After 100 cycles, the specific capacitance was 44% of the first cycle as the 100th cycle yielded the charge capacitance of 14.53 mAh/g. This result shows the 1 hour MnO$_2$ under LT condition to have a low long-term stability as the sample structure was decomposing in the used voltage range.

Table 4.9: Capacitance values of the 1hr α-MnO₂ at LT conditions

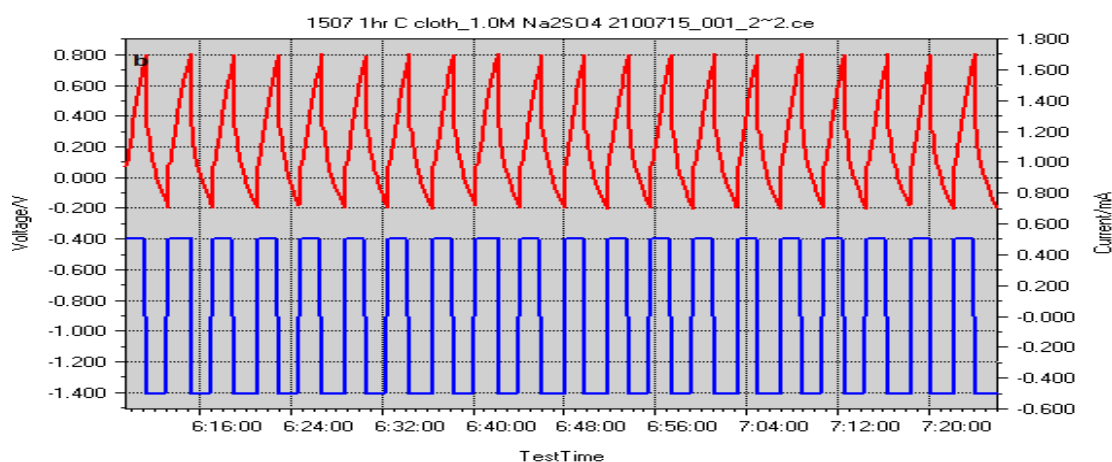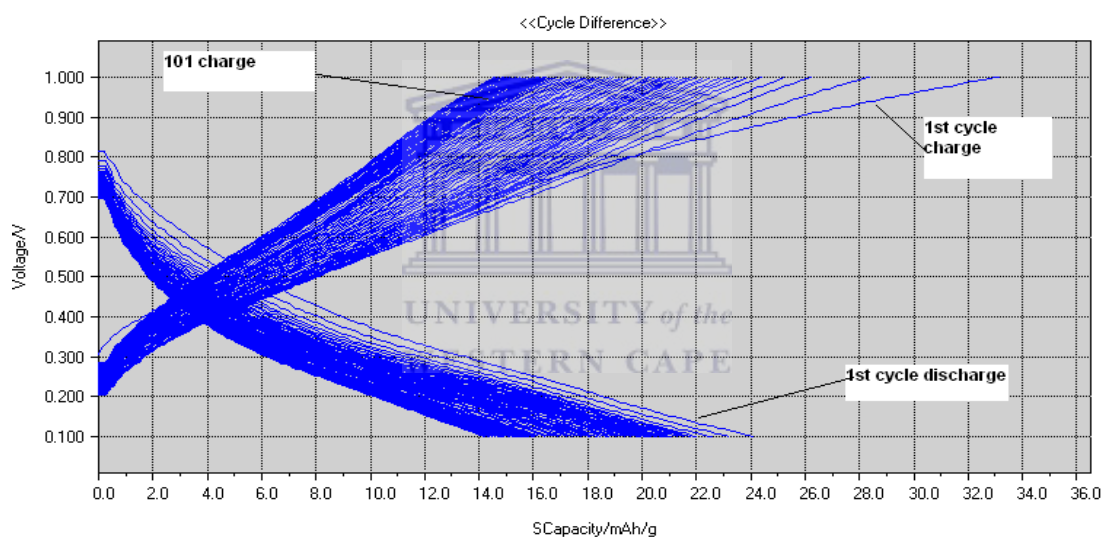| Cycle Number	Charge Capacity (mAh/g)	Charge Capacitance (F/g)	Discharge Capacity (mAh/g)	Discharge Capacitance (F/g)	Cycle efficiency
1	33.11	132.44	24.10	96.40	73%
2	28.13	112.52	23.01	92.04	82%
100	14.53	58.12	14.49	57.96	99.7%

Figure 4.17: *Cycle life of the α-MnO₂ electrode at current of 200μA in 1M of Na₂SO₄ between 0.1 and 1.0 V prepared for 1hr under HT conditions; the above one represents the specific capacitance cycle life for 100cycles.*

Chapter 4: Results and Discussions

The cycle life of the 3 hour MnO_2 under LT conditions is presented in Figure 4.18. As it can be observed from Figure 4..8(a) that it took over 10minutes for the charge and discharge cycles to reach 100 cycles. As it can be observed in Table 4.10 after first cycle the charge and discharge of 67.89 and 26.13mAh/g were obtained respectively, with the cycle efficiency of 38.5%. The second cycle gives capacitance of 38.12 mAh/g and 25.25 mAh/g with cycle efficiency of 66%.

The 100th cycle reversible charge and discharge capacities obtained for 3 hour LT MnO_2 were 24.17 mAh/g and 18.32 mAh/g respectively, giving 76% cycle efficiency for the 100th cycle. With charge capacitance recovery of 36% of the first cycle after 100 cycles, the 3 hour LT MnO_2 has a low long-term stability to be a good material for supercapacitors, as the material decomposes under the potential range of 0.1 and 1.0V. But with initial specific capacitance of 271.56 F/g was promising material.

Table 4.10: Capacitance values of the 1hr α-MnO_2 at LT conditions

Cycle Number	Charge Capacity (mAh/g)	Charge Capacitance (F/g)	Discharge Capacity (mAh/g)	Discharge Capacitance (F/g)	Cycle efficiency
1	67.89	271.56	26.13	104.52	38.5%
2	38.12	152.48	25.25	101.00	66%
100	24.17	96.68	18.32	73.28	76%
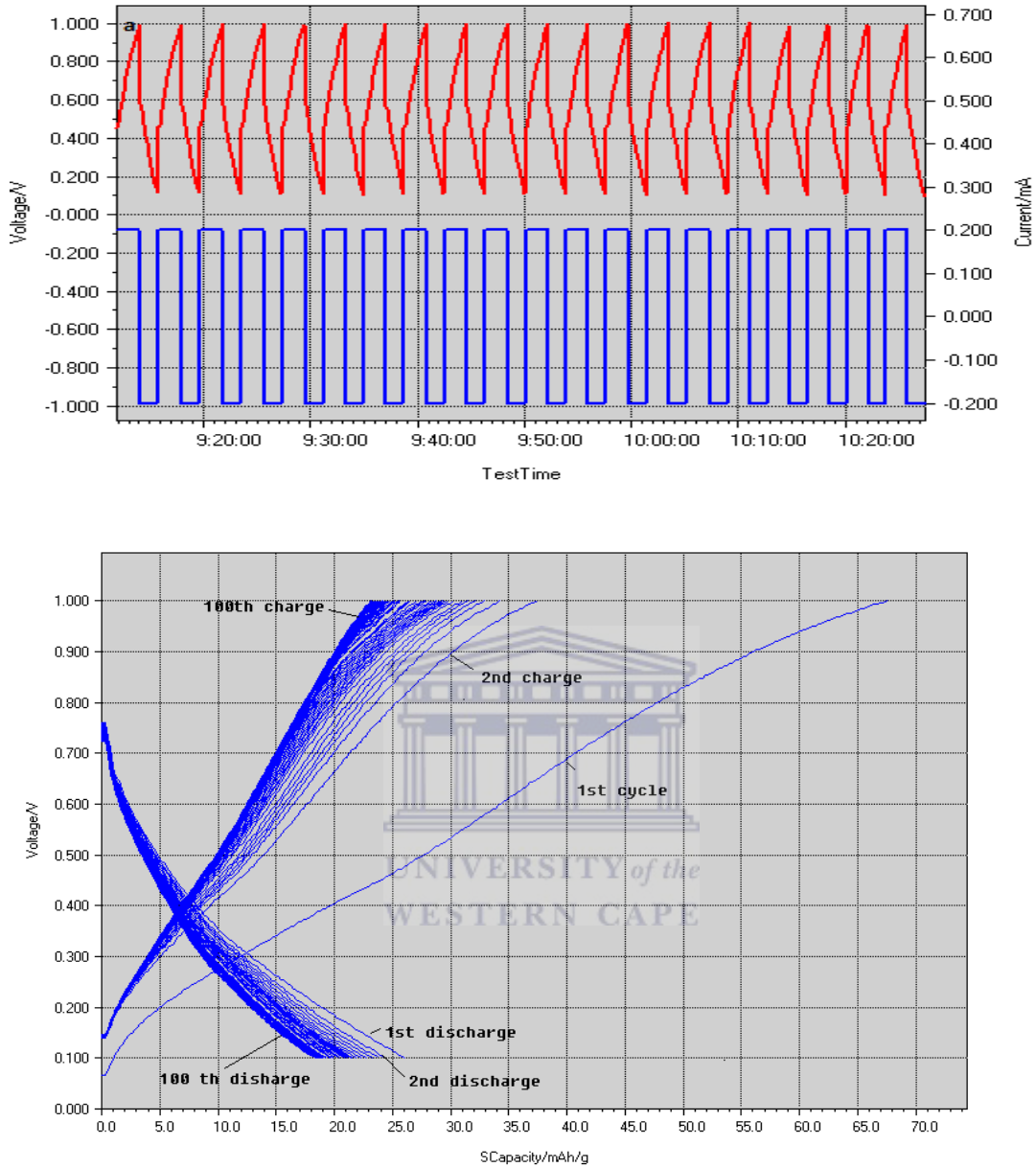
Figure 4.18*: (a) Cycle life of the α-MnO₂ electrode at current of 200μA in 1M of Na₂SO₄ between 0.1 and 1.0 V prepared for 3hr under LT conditions; (b) shows the breaking down of the specific capacitance per each cycle until 100cycles.*

The long term stability of the 6 hour MnO_2 under LT condition, and its variation of specific capacitance is depicted in Figure 4.19. The charge and discharge specific capacitance of the first cycle obtained was 33.13 and 32.18 mAh/g respectively, with a cycle efficiency of 97%. The second cycle yielded the charge and discharge of 32.89

and 31.79 mAh/g respectively, with the cycle efficiency of 96.7%. The specific capacitance of the 6 hour LT MnO_2 after 100 cycles was only 30% of the first cycle. This demonstrates that the materials had poor long term stability unlike those reported in the literature. The α-MnO_2 nano-structured materials prepared under low temperature resulted in not impressive stability, meaning the structural features of the materials were not stable which could be a result of the electrolyte used (1M Na_2SO_4).

Table 4.11: Capacitance values and cycle efficiency of the 6hr LT MnO₂

Cycle Number	Charge Capacity (mAh/g)	Charge Capacitance (F/g)	Discharge Capacity (mAh/g)	Discharge Capacitance (F/g)	Cycle efficiency
1	33.13	132.52	32.18	128.72	97%
2	32.89	131.56	31.79	127.16	97%
100	9.79	39.16	9.79	39.16	100%
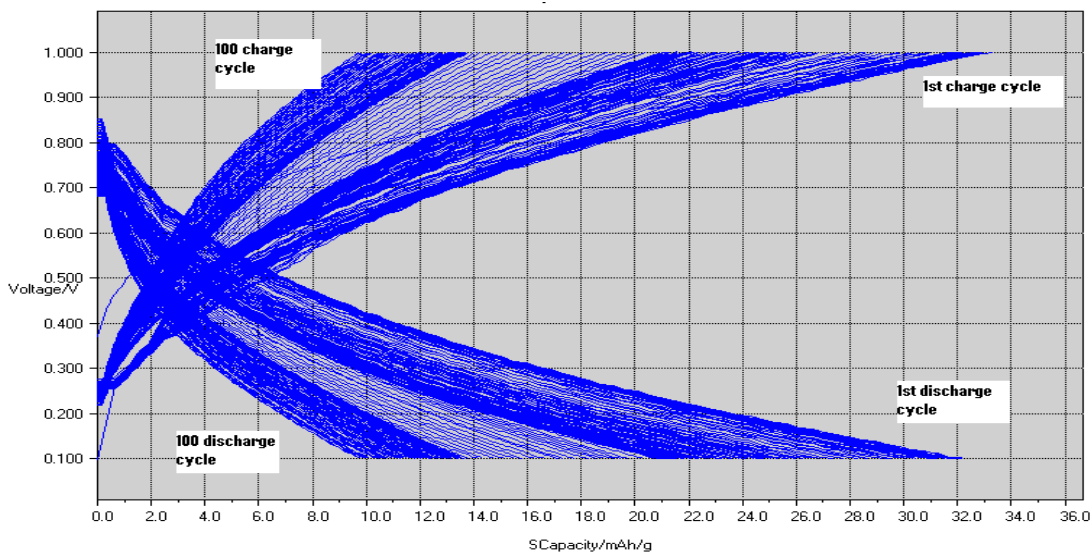
Figure 4.19: *Specific capacitance cycle life of the 6hr LT MnO₂, with 1M Na₂SO₄.*

4.4.2.3 Charge-discharge test of the commercial MnO$_2$

The charge and discharge test was conducted for the commercial γ-MnO$_2$, which is reported to be the least stable polymorph of MnO$_2$ by Tang *Et Al [69]*. Figure 4.20 shows the constant current charging and discharging and behaviour of commercial MnO$_2$ at current density of 200µA. During the charging and discharging steps, the charge curves are very symmetric to their discharge counterparts in the whole potential region and the slope of every curve is potential-independent and maintain a constant value. The cycles of specific capacitance are plotted automatically and are represented by Fig. 4.20b.

The first cycle charge and discharge capacities obtained were 24.5 mAh/g and 15.2 mAh/g respectively, giving cycle efficiency of 62.1%. The second cycle gives capacitance of 17.1mAh/g and 14.9 mAh/g with cycle efficiency of 87.1%. The 100th cycle reversible charge and discharge capacities obtained for 1 hour HT MnO$_2$ were 11.7 mAh/g and 11.6 mAh/g respectively, giving 99.1% cycle efficiency for the 100th cycle. After 100 cycles, the capacitance is only about 17% of the first cycle.

Table 4.12: Capacitance values and cycle efficiencies of commercial MnO$_2$

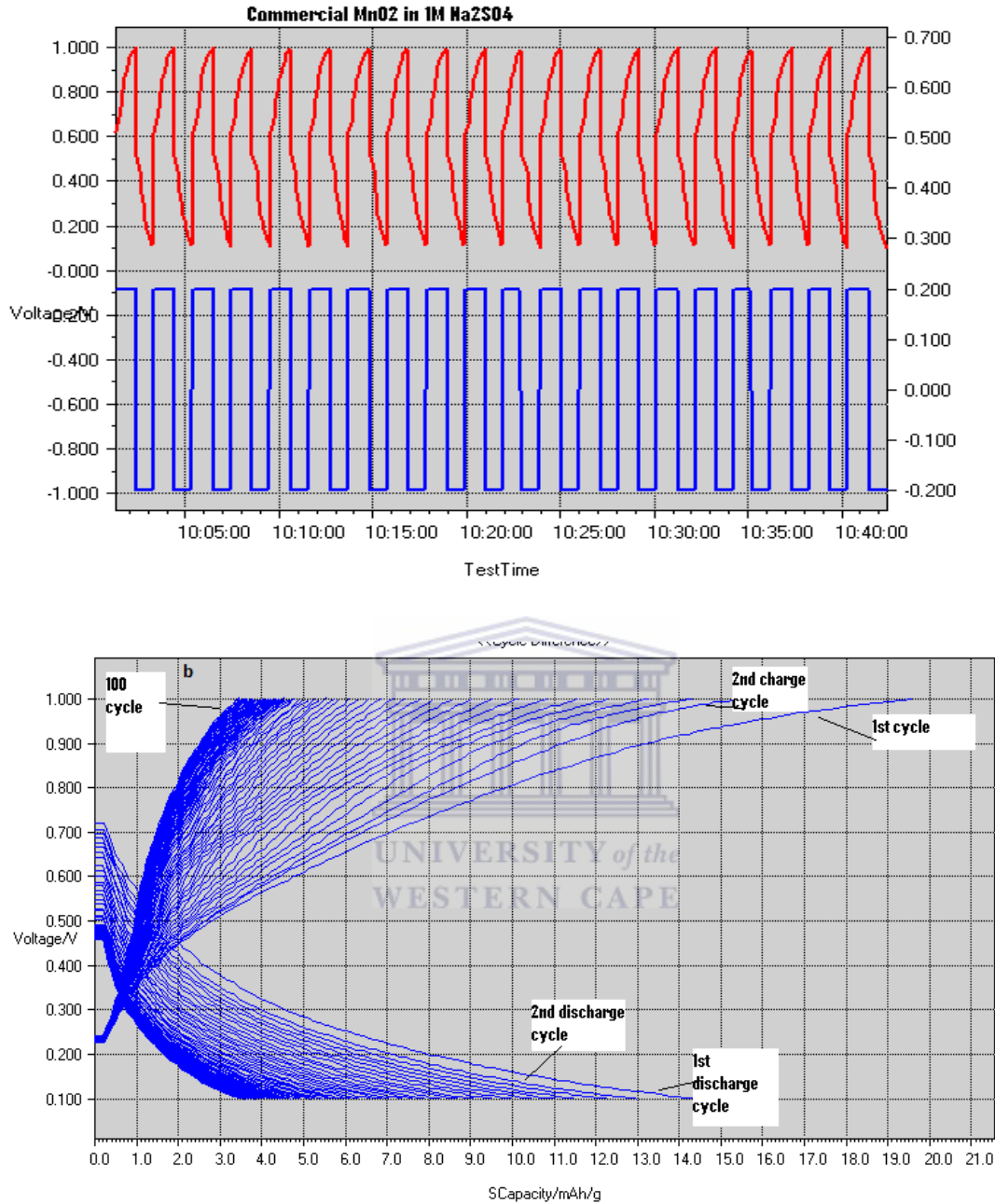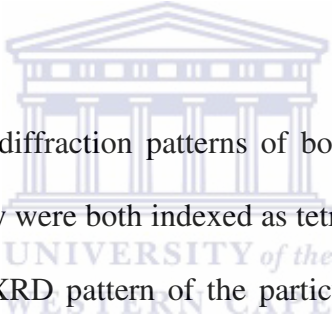| Cycle Number	Charge Capacity (mAh/g)	Charge Capacitance (F/g)	Discharge Capacity (mAh/g)	Discharge Capacitance (F/g)	Cycle efficiency
1	19.60	78.40	14.42	57.68	73.6%
2	15.46	61.84	13.01	52.04	84.1%
3	14.34	57.36	12.27	49.08	85.6%
100	3.40	13.60	3.40	13.60	100%

Figure 4.20: *The charge and discharge of the commercial γ-MnO₂ at constant current 200μA; (b) Cycle life of the commercial MnO₂ in 1M Na₂SO₄ between 0.1 and 1.0V*

Chapter 5: Conclusions and Recommendations.

5.1 Conclusion

In summary, different nanostructured manganese oxides have been synthesised under different conditions namely, low temperature and hydrothermal conditions. Different nanostructures were synthesised by varying the reaction time and keeping the temperature constant. The overall objective was to study the characteristics of the nanostructured electrode material by using both qualitative and quantitative tools. The commercial MnO_2 was also used for comparison with the as-synthesised MnO_2 electrode materials.

As observed from the XRD diffraction patterns of both synthesised nanostructured MnO_2 electrode materials they were both indexed as tetragonal α-MnO_2, with patterns matching with the standard XRD pattern of the particular polymorph of the MnO_2. The patterns showed that by optimising the reaction time did not have much effect on the crystal structure as the patterns and intensities of peaks were more or less similar. The XRD patterns of the MnO_2 under hydrothermal conditions showed peaks that were weak and poorly developed, which could be the result of loss of water contents which can cause variation in crystal lattice. The patterns of the MnO_2 material synthesised under low temperature were very clear which showed the pure crystalline material. The XRD patterns of the commercial MnO_2 were indexed as γ-MnO_2, which is the most unstable polymorph of the MnO_2, it can transform into β-MnO_2.

The morphological features of the electrodes were studied with the SEM and the TEM, and the SEM pictures showed growth of nanorods with the length of 0.5-1µm for the LT MnO_2 and 1-2µm for the hydrothermal MnO_2. The SEM could not spot the

difference in the aggregation states of the optimal samples. The TEM images revealed some minor evolutions in the nanostructures of the optimised samples; the increase in the hydrothermal reaction time was reducing the agglomerations of the nanorods for the HT MnO_2. As explained earlier that the loss in water content had an effect on the structure of the material. The elemental decomposition of the samples revealed some traces of reagents that were used. The commercial MnO_2 was pure with no elemental traces. The TEM images of LT MnO_2 showed no difference in optimal samples, as the agglomerations remained similar. The commercial MnO_2 had spheres like structures as observed by the both SEM and the TEM.

The water loss of the hydrothermal MnO_2 resulted in lower value of the surface area as determined by the BET. The 3 hour sample showed the lowest value of $33.45m^2/g$, whereas the 6 hour sample gave the highest specific surface area of $60.17m^2/g$. The evolement of morphologies during the optimal hydrothermal reaction time causes these varying values. The BET surface area values of the low temperature prepared α-MnO_2 were more or less similar, as the morphologies of both samples were also showing no evolving with varying reaction time.

The pseudo-capacitance properties of the prepared and commercial MnO_2 were studied by cyclic voltammetry and charge-discharge test, and the results showed α-MnO_2 prepared at different low temperature times shows fine capacitive behaviour making them ideal candidates as supercapacitors electrodes. The MnO_2 prepared at 6 hour showed maximum capacitive behaviour of 178.6F/g which makes it an ideal electrode for supercapacitors. The Cycle profile exhibited by the α-MnO_2 prepared under low temperature was not good with the 1 hour exhibiting 44%; the 3 hour yielded 36% and the 6 hour exhibiting only 30% of initial capacity of 100 cycles. The capacitive behaviour of the α-MnO_2 prepared under hydrothermal conditions was low,

with the 3 hour sample recording the lowest capacitive behaviour of 38.36 F/g. But the cycle profile of these electrodes was ideal as they exhibited very good long term stability. The 1 hour sample exhibited the ideal long term stability with 70% of the initial capacity, whereas the 6 hour sample exhibited 63% of the initial capacity; hence this long term stability makes these electrodes ideal candidates for supercapacitor applications [69].
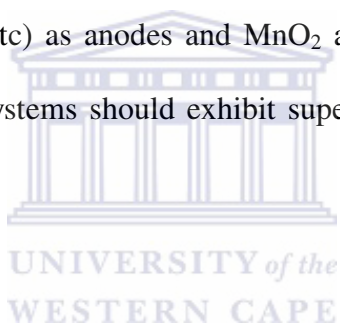
The commercial γ-MnO_2's capacitive behaviour was optimised by using different scan rates of 5mV/s and 50mV/s rates; with the slowest rate exhibiting the ideal capacitive behaviour of 88.1F/g. However, the electrode exhibited a very poor cycle profile, keeping only 17% of the initial capacity after 100 cycles. In final summary and conclusion, the α-MnO_2 synthesised under low temperature conditions achieved an ideal capacitive behaviour but the long term stability was not ideal for them being installed as electrode materials for supercapacitors, whereas the hydrothermally prepared α-MnO_2 yielded a low capacitive behaviour, but their long term stability made them ideal candidates for supercapacitors. In the following chapter, the possible future works and recommendations on how to improve the characteristics and behaviour of the electrode materials will be discussed.

5.2 Future Works and Recommendations

Based on the analysis and conclusion of this study, a number of suggestions regarding priorities of future research directions and are of investigation are listed:

➤ Employ the quantitative technique like thermogravimetric analysis (TGA) in order to find the amount of water present and also observe structural transformation of the MnO_2.

➤ Ideally, the slower scan rate (1mV/s to 5mV/s) is more feasible in order to achieve the ideal capacitive behaviour

➤ Compare different electrolytes like NaCl, KOH, KCl etc, as MnO_2 behaves differently to every cation or anion.

➤ The main recommendation from this study is to employ other materials like highly activated carbon (e.g CNTs, graphite etc) and conducting polymers (e.g PANI, PEDOT etc) as anodes and MnO_2 as cathode when assembling cells. These hybrid systems should exhibit superior capacitive behaviour in comparisons.

References

[1]. K.S. Ryu, K.M. Kim, N.-G. Park, Y.J. Park, S.H. Chang, J. Power Sources **103** (2002) 305.

[2]. H.Y. Lee, J.B. Goodenough, J. Solid State Chem**. 144** (1999) 220.

[3]. B.J. Lee, S.R. Sivakkumar, J.H. Kim, S.H. Jo, D.Y. Kim, J. Power Sources 168 (2007) 546.

[4]. K. Lotaa, V. Khomenkob, E. Frackowiak Journal of Physics and Chemistry of Solids 296 65 (2004) 295–301

[5]. B. Muthulakshmi, D. Kalpana, S. Pitchumani, N.G. Renganathan, J. Power Sources 158 (2006) 1533.

[6]. M. Mastragostino, C. Arbizzani, F. Soavi, Solid State Ionics 148 (2002) 493.

[7]. K.S. Ryu, Y.-G. Lee, Y.-S. Hong, Y.J. Park, X.Wu, K.M. Kim, M.G. Kang, N.-G. Park, S.H. Chang, Electrochim. Acta 50 (2004) 843.

[8]. K.R. Prasad, N. Munichandraiah, J. Power Sources 112 (2002) 443.

[9]. T.C. Girija, M.V. Sangaranarayanan, J. Power Sources 156 (2006) 705.

[10]. C. Arbizzani, M.C. Gallazzi, M. Mastragostino, M. Rossi, F. Soavi, Electrochem.Commun. 3 (2001) 16.

[11]. D. Belanger, X. Ren, J. Davey, F. Uribe, S. Gottesfeld, J. Electrochem. Soc.147 (2000) 2923

[12] P. Simon, Y. Gogotsi. Materials for electrochemical capacitors. Nat. Mater. 2008, 7, 845

[13]. D. Belanger, T. Brousse and J.W. Long: The electrochemical society interface (2008)

References

[14]. J. Miller, A brief history of Supercapacitors, (2007) 61

[15]. M. Winter, R.J. Brodd. What are batteries, fuel cells and supercapacitors? Chem. Rev. 2004, 104, 4267

[16]. T. L. Wade: High Power Carbon-based supercapacitors, (2006)

[17]. Post J E 1999 *Proc. Natl Acad. Sci. USA* **96** 3447

[18]. T. Gao, H. Fjellvag, P. Norby. Structural and morphological evolution of β-MnO_2 nanorods during hydrothermal synthesis. Nanotechnology. **20**, (2009) 1

[19]. S.W. Zhang, G.Z. Chen. Manganese oxide based materials for supercapacitors. Review, 3, (2008) 186-199

[21]. J.R. Miller, P. Simon. Fundamentals of electrochemical capacitor design and operation. The electrochemical society, (2008) 31-32

[22]. A. A. Francis and C. Forsyth: available at:

http://rais.ornl.gov/tox/profiles/mn.shtml (accessed 12 October 2008).

[23]. H. Y. Lee and J. B. Goodenough: J. Solid State Chem., 1999, **144**, 220–223.

[24]. S.-C. Pang, M. A. Anderson and T. W. Chapman: J. Electrochem. Soc., **2000**, 147, 444–450.

[25]. M. Toupin, T. Brousse and D. Belanger: Chem. Mater., 2002, **14**, 3946–3952.

[26]. M. Toupin, T. Brousse and D. Belanger: Chem. Mater., 2004, **16**, 3184–3190.

[27]. M. Nakayama, A. Tanaka, Y. Sato, T. Tonosaki and K. Ogura: Langmuir, 2005, **21**, 5907–5913.

[28]. A. J. Bard and L. R. Faulkner: 'Electrochemical methods: fundamentals and applications'; 2001, New York, John Wiley & Sons.

[29]. S. L. Kuo and N. L. Wu: J. Electrochem. Soc., 2006, **153**, A1317–A1324.

References

[30]. J. K. Chang, M. T. Lee and W. T. Tsai: J. Power Sources, 2007, **166**, 590–594.

[31]. J. Li and I. Zhitormirsky*: J. Mater. Process. Technol.*, 2008, In press.

[32]. Y. S. Chen, C. C. Hu and Y. T. Wu*: J, Solid State Electrochem.* **8**, (2004) 467-473

[33]. K. Rajendra Prasad and N Miura: *Electrochem. Commun*, **6**, (2004) 1004-1008

[34]. J. N. Broughton and M.J. Brett*: Electrochem. Acta***, 49**, (2004) 4439-4446

[35]. J. J. Xu, A. J. Kinser, B. B. Owens and W. H Smyrl*: Electrochem. Solid-state Lett*, **1**, (1998) 1-3

[36]. C. Y. Chen, Y. R. Lyu, C. Y. Su, H. M. Lin and C. K. Lin: *Surf. Coat. Technol,* 202, (2007) 1277-1281

[37]. Y. Dai, K. Wang and J. Xie: *Appl. Phys. Lett*, 90, (2007) 104102-104103

[38]. K. W. Nam and K. B. Kim: *J. Electrochem. Soc***, 153**, (2006) A81-A88

[39]. T. Brousse, M. Toupin, R. Douglas, L. Athouel, O. Crosnier and D. Belanger: *J. Electrochem. Soc***, 153**, (2006) A2171-A2180

[40]. A. Taguchi, S. Inoue, S. Akamaru, M. Hara, K. Watanabe and T Abe: *J. Alloys Compd***, 414,** (2006) 137-141

[41]. S. Devaraj and N. Munichandraiah*: Electrochem. Solid-State Lett*, **8**, (2005) A373-A377

References

[42]. S. Devaraj and N. Munichandraiah: J. Electrochem. Soc, 154, (2007) A901-A909

[43]. H. K. Song, Y. H. Jung, K. H. Lee and L. H. Dao: Electrochem. Acta, 44, (1999) 3513-3519

[44]. J. H. Jang, S. Han, T. Hyeon and S. M. Oh: *J. Power Sources*, **123**, (2003) 79-85

[45]. E. Raymundo-Pinero, V. Khomenko, E. Frackowiak and F. Beguin: *J. Electrochem. Soc*, **152,** (2005) A229-A235

[46]. S. Devaraj and N. Munichandraiah*: J. Electrochem. Soc*, **154**, (2007) A80–A88.

[47]. J. K. Chang, Y. L. Chen and W.T. Tsai: J. Power Sources, 2004,**135**, 344–353.

[48]. B. Djurfors, J. N. Broughton, M. J. Brett and D. G. Ivey: J. Mater. Sci., 2003, **38**, 4817–4830.

[49]. M. Nakayama, A. Tanaka, S. Konishi and K. Ogura*: J. Mater.Res*., **19**, (2004) 1509–1515.

[50]. S. H. Lee, M. S. Hong and S. W. Kim: *Electrochem. Solid-State Lett*, **5**, (2002) A227-A230.

[51]. Y. U. Jeong and A. Manthiram: *J. Electrochem. Soc*, **149**, (2002) A1419–A1422.

[52]. A. Yuan and Q. Zhang: *Electrochem. Commun.* **8**, (2006) 1173–1178

[53]. J. Jiang and A. Kucernack*: Electrochem. Acta*, **47**, (2002) 2381-2386

[54]. K. T. Lee and N. L. Wu: *J. Power Sources*, **179**, (2008) 430-434

[55]. V. Khomenko, E. Raymundo-pinero, E. Frackowiak and F. Beguin: *Appl. Phys. A*, **82A**, (2006) 567-573

[56]. Y. T. Wu, C. C. Hu: J. Electrochem. Soc, **151**, (2004), A2060-A2066

References

[57]. G. X. Wang, B. L. Zhang, Z. L. Yu and M. Z. Qu: *Solid State Ion*, **176**, (2005) 1169-1174

[58]. Z. Fan, J. Chen, M. Wang, K. Cui, H. Zhou and Y. Kuang: Diamond Relat. Mater, 15, (2006) 1478-1483

[59]. T. Brousse, M. Toupin and D. Belanger*: J. Electrochem. Soc*, **151**, (2004) A614-A622

[60]. V. Khomenko, E. Raymundo-Pinero, E. Frackowaik and F. Beguin: Appl. Phys. A, **82A**, (2006) 567-573

[61].Y. Zhang, H. Feng, X. Wu, L. Wang, A. Zhang: International Journal of Hydrogen energy, **34**, (2009) 4889-4899

[62]. F. Jiao and P. G. Bruce: *Adv. Mater,* 19, (2007) 657

[63]. V. Subramanian, H.W. Zhu, R. Vajtai, P.M. Ajayan, B.Q. Wei, J. Phys. Chem. B **109** (2005) 20207.

[64]. R.N. Reddy, R.G. Reddy, J. Power Sources **124** (2003) 300.

[65]. M.W. Xu, D.D. Zhao, S.J. Bao, H.L. Li, J. Solid State Electrochem. **11** (2007) 1101.

[66]. H.Y. Lee, J.B. Goodenough, J. Solid State Chem. **144** (1999) 220.

[67]. T. Xue, C.L. Xu, D.D. Zhao, J. Power Sources **164** (2007) 953.

[68]. P. Ragupathy, H.N. Vasan, N. Munichandraiah, J. Electrochem. Soc. **155** (2008) A34.

[69]. N. Tang, X. Tian, C. Yang and Z. Pi: Materials research bulletin, **44**, (2009) 2062-2067

References

[70]. Y. Chen, C. Liu, F. Li and H. Cheng: Journal of alloys and compounds, **397**, (2005) 282-285

[71]. B.X. Li, G.X. Rong, Y. Xie, L.F. Huang, C.Q. Feng, Inorg. Chem. **45** (2006) 6404.

[72]. W. Ostwald, Z. Phys. Chem. **34** (1900) 495.

[73]. S.J. Bao, O.L. Bao, C.M. Li, T.P. Chen, C.Q. Sun, Z.L. Dong, Y. Gan, J. Zhang, Small **3**(2007) 1174.